Remote Sensing of Surface and Cloud Properties in the Arctic from AVHRR Measurements

W. HAN* AND K. STAMNES

Geophysical Institute, University of Alaska, Fairbanks, Fairbanks, Alaska

DAN LUBIN

Scripps Institution of Oceanography, University of California, San Diego, La Jolla, California

(Manuscript received 27 November 1998, in final form 28 August 1998)

ABSTRACT

Algorithms to retrieve cloud optical depth and effective radius in the Arctic using Advanced Very High Resolution Radiometer (AVHRR) data are developed, using a comprehensive radiative transfer model in which the atmosphere is coupled to the snowpack. For dark surfaces AVHRR channel 1 is used to derive visible cloud optical depth, while for bright surfaces AVHRR channel 2 is used. Independent inference of cloud effective radius from AVHRR channel 3 (3.75 μm) allows for derivation cloud liquid water path (proportional to the product of optical depth and effective radius), which is a fundamental parameter of the climate system. The algorithms are based on the recognition that the reflection function of clouds at a nonabsorbing wavelength (such as AVHRR channel 1) in the solar spectrum is primarily a function of cloud optical thickness, whereas the reflection function at a liquid water absorbing wavelength (such as AVHRR channel 3) is primarily a function of cloud particle size. For water clouds over highly reflecting surfaces (snow and ice), the reflectance in AVHRR channel 1 is insensitive to cloud optical depth due to the multiple reflections between cloud base and the underlying surface; channel 2 (0.85 μm) must be used instead for optical depth retrieval. Water clouds over tundra or ocean are more straightforward cases similar to those found at lower latitudes, and in these cases a comprehensive atmospheric radiative transfer model with a Lambertian surface under cloud is used. Thus, for water cloud over tundra and ocean, channel 1 is used for cloud optical depth retrieval. In all cases, channel 3 is used for independent retrieval of cloud droplet effective radius. The thermal component of channel 3 is estimated by making use of channel 4 (11 μm) and is subtracted from the total channel 3 radiance. Over clear-sky scenes, the bidirectional reflectance properties of snow are calculated directly by the coupled snowpack–atmosphere model. This results in greater overall accuracy in retrieved surface properties as compared with the simplified approach that uses a Lambertian approximation for the surface albedo.

To test the physical soundness of the algorithms the authors have applied them to AVHRR data over Barrow, Alaska, from April to August 1992. Downwelling irradiances at the surface calculated using the retrieved cloud optical depth and effective radius are compared with field irradiance measurements, and encouraging agreement is found. The algorithms are also applied to three areas of about 100-km dimension around Barrow, each having a different underlying surface (ocean, tundra, snow).

1. Introduction

The climatic effects of clouds are difficult to estimate due to their temporal and spatial variability. Satellite remote sensing techniques are needed to determine cloud parameters, such as cloud liquid water path and effective radius, on a global scale. Field experiments can provide necessary tests of cloud retrieval algorithms from satellite data. The research on cloud retrieval from remote sensing data has remained active for years (see e.g., Twomey and Cocks 1982, 1989; King 1987; Nakajima and King 1990; Nakajima et al. 1991; Rossow et al. 1989; Platnick and Twomey 1994; Han et al. 1994; Nakajima and Nakajima 1995; Platnick and Valero 1995). These techniques are based on the fact that the reflection function of clouds at a nonabsorbing channel in the visible wavelength range is primarily a function of cloud optical depth, whereas the reflection function at a water absorbing channel in the near-infrared is primarily a function of cloud droplet size.

Most of these cloud retrieval algorithms, however, are applied to dark surfaces at low and midlatitudes. At high latitudes, the surface is covered by snow/ice most of the time throughout the year. Unlike dark surfaces, snow

* Current affiliation: SFA, Inc., Largo, Maryland.

Corresponding author address: Dr. Knut Stamnes, Geophysical Institute, University of Alaska, 903 Koyukuk Drive, P.O. Box 757320, Fairbanks, AK 99775-0800.
E-mail: knut@gi.alaska.edu

surfaces have the same magnitude in albedo as cloud. Solar radiation reflected by the cloud–surface system in the visible is insensitive to cloud optical depth over snow/ice surfaces because of the multiple reflections between cloud base and the underlying snow/ice surface. Much of the light transmitted downward through the cloud is subsequently reflected by the snow. Note, however, that if the cloud is sufficiently thin, most of this reflected light is transmitted upward through the cloud, and only a small fraction of it is reflected back down. Thus, for thin clouds multiple reflections play a minor role. Because of this insensitivity of reflected visible light to cloud optical depth, visible measurements cannot be used to retrieve cloud optical depth over bright surfaces.

Alternatively, the near-infrared channel centered at 0.85 μm acquired with the Advanced Very High Resolution Radiometer (AVHRR) is used to infer water cloud optical depth over snow/ice surfaces in the Arctic (Key 1999). This approach is based on the premise that the reflected solar radiation at 0.85 μm is primarily a function of water cloud optical depth, which is nearly independent of wavelength in the visible and near-infrared regions. Because of the weak wavelength dependence, the cloud optical depth inferred from the near-infrared channel is almost the same as that in the visible. Although use of the 0.85-μm channel makes retrieval feasible, the snow surface is bright also in this channel. As will be shown below, the low contrast between the cloud and the snow surface leads to large errors in retrieved optical properties for thin clouds because of the sensitivity of the retrieved cloud properties to small errors in the measured or modeled radiance. Key (1999) adopted the Lambertian approximation for snow surfaces under cloudy conditions, and he found that multiple solutions occur at small optical depths and large solar zenith angles. Other cloud retrieval methods over snow surfaces include an empirical parameterization for cloud optical depth as a function of the brightness temperature difference between AVHRR channels 3 and 4 (11 μm), which was derived for cloud fields over the ocean and applied to nearby cloud fields over snow and ice, and this technique was applied to three test AVHRR images over Antarctica (Lubin et al. 1994).

Our objective is to develop algorithms, suitable for Arctic conditions, to infer cloud liquid water path (LWP), effective particle radius, and cloud-top temperature from AVHRR images, using a discrete-ordinates radiative transfer formulation in which the atmosphere is coupled to the snowpack. Here we should note that the quantity that can be inferred from AVHRR data (using channel 1 over dark surfaces, and channel 2 over bright surfaces) is cloud optical depth, τ. However, we can easily derive cloud LWP from visible (channel 1) or near-infrared (channel 2) cloud optical depth once we have inferred effective radius, r_{eff}, independently from channel 3, since τ is proportional to LWP and inversely proportional to r_{eff}.

For low albedo surfaces we follow the general approach developed by Nakajima and King (1990), which was later adopted by Nakajima and Nakajima (1995) and Platnick and Valero (1995). For high albedo surfaces our approach is similar to that of Key (1999), with one important exception. Key assumes that the surface is a Lambertian reflector, while we employ a radiative transfer model that couples the atmosphere to the snowpack in order to incorporate more correctly the bidirectional reflectance properties of snow. This becomes important for high albedo surfaces and, as we shall see below, incorporation of this coupling produces significantly better results than the Lambertian approximation. Another new feature of our approach is that we employ a radiative transfer model that is specifically tailored to arctic conditions and that has been thoroughly tested against data collected during the Arctic Stratus Cloud Experiment conducted over the Beaufort Sea in 1980 (Tsay et al. 1989).

The data and physical models are introduced in sections 2 and 3, respectively. In section 4, algorithms to infer ground surface properties, such as albedo and snow particle size, are described, then applied to AVHRR data collected in the Arctic, and tested against ground-based measurements. In section 5, algorithms to retrieve optical depth and effective radius of liquid water clouds are described, validated using in situ irradiance measurements, and applied to AVHRR images for three different arctic surface types: ocean, tundra, and snow. A summary is provided in section 6.

2. Satellite and field data in the arctic

The National Oceanic and Atmospheric Administration (NOAA) polar orbiter data used for this study were tracked from Elmendorf Air Force Base (Alaska) during 1992, archived as digital high-resolution picture transmission (HPRT) data at the Arctic and Antarctic Research Center (AARC) at Scripps Institution for Oceanography, and processed by the TeraScan software (SeaSpace, Inc.) installed at the Alaska Data Visualization and Analysis Laboratory. AVHRR is a cross-tracking system, featuring five channels. The instantaneous field of view (IFOV) of each channel is approximately 1.4 milliradians leading to a resolution at the satellite subpoint of 1.1 km for a nominal altitude of 833 km. More details on the AVHRR instrumentation are given by Kidwell (1995).

The absolute radiometric responsivities of the AVHRR visible (channel 1, centered at 0.65 μm) and near-infrared (channel 2, centered at 0.85 μm) channels, for which there are no onboard calibration capabilities, are known to change from the NOAA-reported prelaunch values once the sensor is in orbit and continue to drift over time.

Several efforts have been made to estimate the degradation rates through ground-based experimental techniques (Brest and Rossow 1992; Kaufman and Holben

1993; Rao and Chen 1995). As part of the National Aeronautics and Space Administration's (NASA) AVHRR Pathfinder program, investigations of Rao and Chen indicated that the relative annual degradation rates for the two channels are 1.2% and 2.0% (*NOAA-11*), respectively. In this study we adopt Rao and Chen's postlaunch calibration equations, which have been recommended to users by the NOAA/NASA AVHRR Pathfinder Calibration Working Group, as follows:

$$R_1 = 0.5496[C_{10}(1) - 40] \exp(0.33 \times 10^{-4} d) \quad (1)$$

$$R_2 = 0.3680[C_{10}(2) - 40] \exp(0.55 \times 10^{-4} d), \quad (2)$$

where R_1 and R_2 are calibrated radiances for each channel in W m^{-2} sr^{-1} μm^{-1}, d is the day after launch, and $C_{10}(1)$ and $C_{10}(2)$ are measured signals in 10-bit counts for channel 1 and 2, respectively. For *NOAA-10*, we adopt postlaunch calibration coefficients suggested by Teillet et al. (1990) in the following formulas:

$$R_1 = \frac{C_{10}(1)}{1.61} - \frac{35.3}{1.61} \quad (3)$$

$$R_2 = \frac{C_{10}(2)}{2.10} - \frac{33.8}{2.10}. \quad (4)$$

Surface solar radiation measurements in Barrow, Alaska (71°18′N, 156°47′W), are provided by Climate Monitoring and Diagnostics Laboratory (CMDL) of NOAA. Broadband solar radiation measurements by Eppley pyranometers, covering the wavelength range 0.3–2.8 μm, include upward and downward global solar irradiances. The uncertainty in the measurements is less than 2.3% (Latimer 1972). The hourly averaged measurements from April to August 1992 are used in this study for comparison with the satellite-derived irradiances. The CMDL pyranometers are calibrated anually at the NOAA/CMDL laboratory in Boulder, Colorado.

3. Radiative transfer model

Radiative transfer models form the theoretical basis of cloud retrieval algorithms. We use a comprehensive radiative transfer model that considers radiative interactions with atmospheric gases, such as CO_2, O_3, O_2, and water vapor, and scattering and absorption/emission by stratospheric aerosols, haze particles, and tropospheric aerosols. Radiative transfer simulations are carried out by a discrete-ordinates method applied to a plane-parallel vertically inhomogeneous atmosphere–earth system (Stamnes et al. 1988), which has previously been used for rigorous theoretical studies of both the troposphere and stratosphere (e.g., Tsay et al. 1989; Stamnes and Tsay 1990; Wang and Lenoble 1994; Zeng et al. 1994; Forster and Shine 1995). For computational efficiency the exponential-sum fitting of transmissions (ESFT) method is adopted to simulate the gaseous absorption in a multiple scattering atmosphere. Molecular scattering is computed from Rayleigh scattering theory (Penndorf 1957). In this study, a subarctic model atmosphere (McClatchey et al. 1971) is employed. The atmosphere is divided into 33 layers vertically. For snow-free conditions (tundra or ocean) an albedo is assigned to the surface, while an additional layer is added at the bottom of the atmosphere to represent snow overlying tundra (or sea ice).

The solar spectrum from 0.28 to 4 μm is divided into 24 bands with unequal spectral widths that vary from 240 to 3040 cm^{-1}. In the thermal spectral region for wavenumbers less than 2500 cm^{-1} the bandwidth is 20 cm^{-1}. Using this model we can compute irradiance and radiance at any depth, for any combination of individual bands as well as for the entire solar spectral range. For irradiance computations integrated across the solar spectrum, it has been shown that the accuracy of this broadband model is a few watts per meter squared compared with a narrowband model for which the spectral width is less than 100 cm^{-1} (Tsay et al. 1990). The computed radiance is weighted by the spectral response function of each channel (Kidwell 1995). Three types of aerosol, liquid water cloud, and snow/ice included in the model are described in the following sections.

a. *Arctic haze and stratospheric and tropospheric aerosols*

Haze in the Arctic atmosphere can reduce downward shortwave fluxes at the surface by 10–12 W m^{-2} and upward fluxes at the TOA by 6 W m^{-2} in summertime under cloud-free condition with low relative humidity (Tsay et al. 1989). Arctic haze concentration varies seasonally with a maximum in late spring and a minimum in late summer (Shaw 1982). It appears vertically distributed in multiple layers within 3 km above the surface (Valero et al. 1983), and observations indicate that it contains a substantial amount of anthropogenic compounds like sulfuric acid and soot. Blanchet and List (1983) built a sophisticated physical model to calculate the optical properties of Arctic haze from Mie theory. Tsay et al. (1989) parameterized the optical properties of Arctic haze as a function of relative humidity through a least squares fitting based on Blanchet and List's model. In the present study the optical depth is taken to lie between 0.06 and 0.16 at 0.50 μm, for summer and spring, respectively, to agree with available measurements (Shaw 1982).

Following the eruptions of Mount Pinatubo (14 Jun 1991), decreases of 25%–30% in direct solar irradiance were recorded by the NOAA/CMDL pyrheliometers, and derived monthly average aerosol optical depth anomalies at Barrow reached nearly 0.3 during summer of 1992 (Dutton and Christy 1992). Being mainly of volcanic origin, the stratospheric aerosol layer is usually situated between 10 and 30 km, and it is composed primarily of sulfuric acid solution droplets, which are produced through photochemical reactions (Turco et al. 1982). Shettle and Fenn (1976) summarized four dif-

ferent vertical profiles of the extinction coefficients for background, moderate, high, and extreme volcanic aerosol loading situations with the size distributions represented by a ''fresh volcanic model'' and an ''aged volcanic model.'' We have chosen the profile corresponding to doubled high volcanic aerosol loading and the fresh volcanic model to represent the stratospheric aerosols over Barrow, Alaska, after the eruption of Mount Pinatubo. These choices lead to an optical depth of the stratospheric aerosols over Barrow, Alaska, of 0.19 at 0.55 μm, in agreement with CMDL measurements during 1992.

In the troposphere from 3 to 10 km, a tropospheric aerosol model proposed by Shettle and Fenn (1976) is adopted. These aerosols are assumed to have the composition of 70% water soluble and 30% dustlike. The optical depth of the tropospheric aerosol is 0.07 at 0.55 μm.

The total optical depth of the aerosol (counting all three types of aerosol) is 0.42 for spring and 0.32 for summer. These values are higher than normal due to the eruption of Mount Pinatubo. The evidence of the effect of the eruption of Mount Pinatubo on arctic aerosols is also found in Resolute Passage in the Canadian Archipelago, where the optical depth of aerosol derived through a Sun photometer and model calculations for 13 May 1992 is 0.303 (de Abreu et al. 1994). For lack of better knowledge the Henyey–Greenstein phase function (Henyey and Greenstein 1941) is adopted in this paper to represent aerosol particles.

b. Water cloud

Cloud effective radius (r_e, μm) is defined as

$$r_e = \frac{\int n(r) r^3 \, dr}{\int n(r) r^2 \, dr}, \tag{5}$$

where $n(r)$ is the cloud droplet size distribution.

Another quantity characterizing cloud microphysics is the liquid water content (LWC, g cm^{-3}), defined as follows:

$$\mathrm{LWC} = \frac{4\pi\rho_w}{3} \int n(r) r^3 \, dr, \tag{6}$$

where ρ_w (g cm^{-3}) is the density of water. The cloud droplet effective radius r_e and the liquid water content LWC can be parameterized in terms of the single scattering albedo a, the extinction coefficient k, and the asymmetry factor g, as follows (Hu and Stamnes 1993):

$$\frac{k}{\mathrm{LWC}} = a_1 r_e^{b_1} + c_1 \tag{7}$$

$$1 - a = a_2 r_e^{b_2} + c_2 \tag{8}$$

$$g = a_3 r_e^{b_3} + c_3. \tag{9}$$

The coefficients a_i, b_i, and c_i are wavelength dependent, but a small table of coefficients replaces extremely time-consuming Mie computations (Hu and Stamnes 1993). Cloud optical depth is defined as

$$\tau = \int_{z_1}^{z_2} k \, dz, \tag{10}$$

where z_1 is the cloud base and z_2 is the top. The liquid water path is simply LWP = LWC$(z_2 - z_1)$ if the LWC is assumed to be independent of z.

The cloud LWC is explicitly used in the radiative transfer model, but it cannot be directly retrieved from satellite data. Cloud optical depth is proportional to LWP and inversely proportional to the effective radius in the visible. Since the optical depth τ and effective radius can be derived from satellite data, we can estimate the liquid water path.

c. Boundary conditions

Ocean and tundra surfaces are treated as Lambertian (isotropic) reflectors while snow/ice surfaces are included as one additional vertical layer when we carry out radiative transfer calculations. Lacking knowledge of the bidirectional reflectance for tundra, we thus adopt the Lambertian approximation. This is justifiable because the albedo of tundra is low.

Field measurements and model simulations indicate that snow exhibits significant bidirectional reflectance properties, which are more pronounced at larger solar zenith angles (e.g., Grenfell et al. 1994, their Fig. 13; Brandt et al. 1991, their Fig. 1; Han et al. 1993). Because snow is a highly anisotropic reflector, the Lambertian approximation could lead to substantial errors. Therefore, we employ the optical properties of pure snow obtained by Wiscombe and Warren (1980) and Warren and Wiscombe (1980) through Mie computations, and treat snow as one additional vertical layer when we carry out the radiative transfer calculations. The most important variable controlling snow albedo is the mean grain size. The average grain radii are in the range 20–100 μm for new snow, 100–300 μm for fine-grained older snow, and 1000–1500 μm for old snow near the melting point. A Lambertian surface is assumed under the snow layer, but in practice, unless the snow layer is very thin, it will act as a semi-infinite layer.

The Mie scattering approximation assumes that the snow particles are smooth spheres that are not in close physical proximity. At visible and near-infrared wavelengths the snow particle sizes and spaces between them are large compared to the wavelength of light as pointed out by Grenfell et al. (1994). Reasons why Mie theory is acceptable for nonspherical particles that are large compared to the wavelength of light have been put forward by C. Bohren [quoted by Grenfell et al. (1994)] as follows: (i) the orientationally averaged extinction cross section of a convex particle is one-half its surface

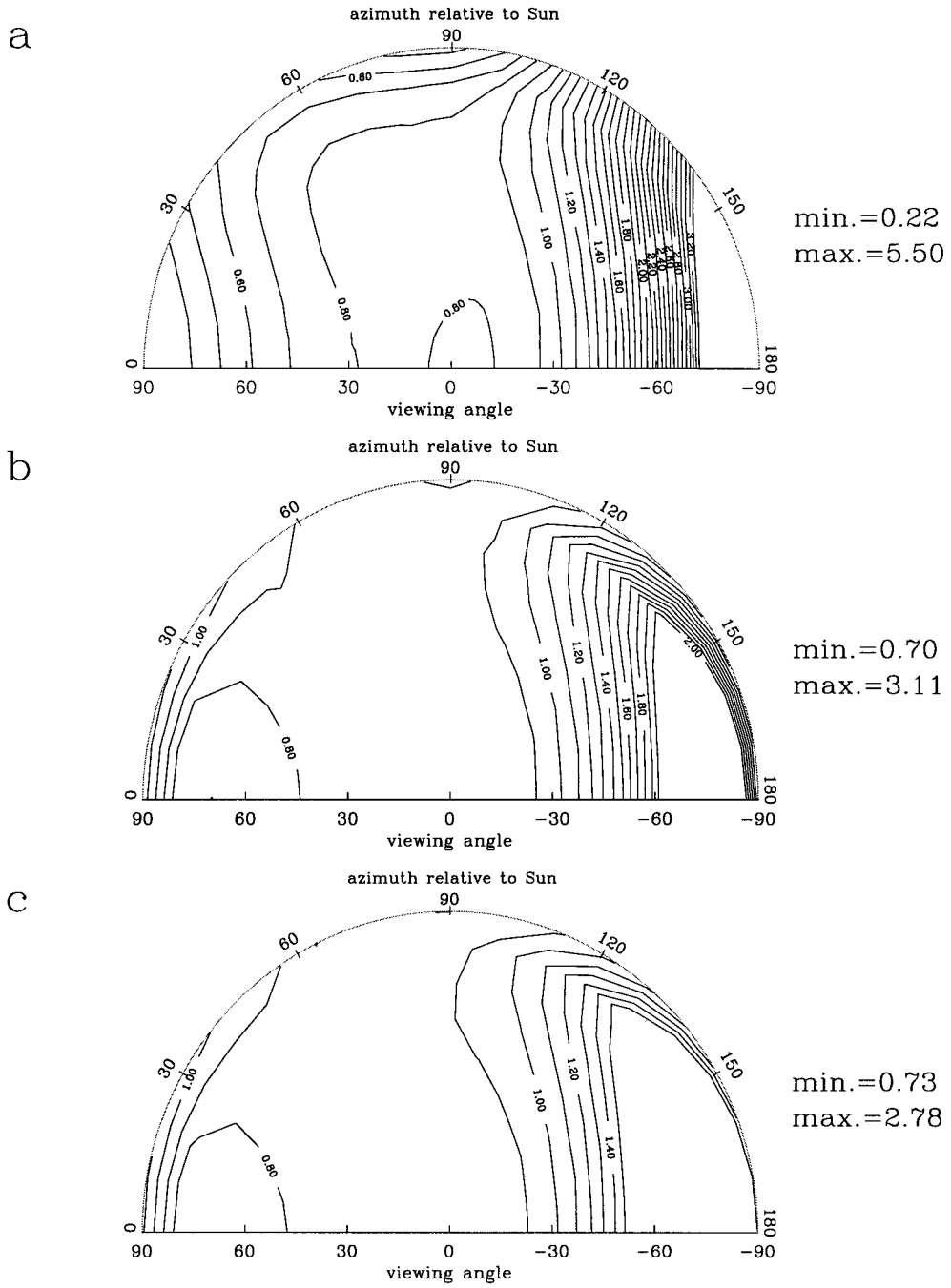

FIG. 1. Contour plots of simulated anisotropic reflectance factor in AVHRR channel 1 (for $\theta_0 = 70°$) at (a) snow surface without atmosphere, (b) the TOA over snow surface for clear-sky conditions in the absence of haze, and (c) the TOA over snow surface for clear-sky conditions in the presence of haze with optical depth 0.16. Snow grain size is 200 μm. Negative viewing angles mean antisolar side.

area, and the absorption cross section of a nearly transparent particle is proportional to its volume almost independent of shape; (ii) the asymmetry parameter is dominated by near-forward scattering, which does not depend strongly on particle shape.

We note also that Mie theory cannot handle specular reflection properly from an oriented ice surface at the top of the snowpack. Therefore, it is important to choose satellite data with viewing angles away from the direction of the specular reflection.

In the visible region, Warren and Wiscombe (1980) introduced trace amounts of absorptive impurities such

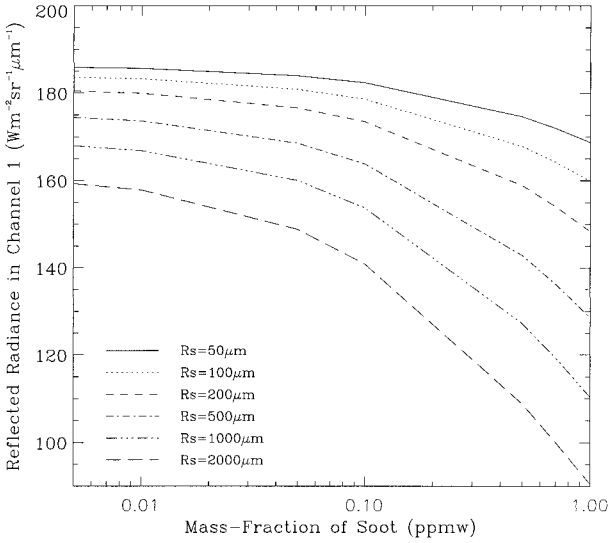

FIG. 2. Simulation of reflected solar radiances in AVHRR channel 1 as a function of the mass fraction of soot and snow grain size for solar zenith angle $\theta_0 = 60°$, satellite zenith angle $\theta = 10°$, and relative azimuth angle between the sun and the satellite $\phi = 50°$.

as graphitic carbon for soot-contaminated snow. In the infrared region the albedo of pure snow remains the same as that for soot-contaminated snow due to the high imaginary refractive index of ice throughout the infrared. For a mixture of snow/ice and soot, the optical properties are obtained by properly weighting each component. The mass fraction of soot ranges from 0.01 to 0.06 ppmw (parts per million by weight) for Arctic snow/ice based on observations (see, e.g., Clarke and Noone 1985, Fig. 2 of Warren and Wiscombe 1985). For soot we have used a 5.74 cross-sectional area per unit mass, which is a typical value for a mixture of graphite and amorphous carbon (Warren and Wiscombe 1980). It is determined by soot grain size and density.

To characterize the anisotropy it is customary to use a bidirectional reflectance distribution function (BRDF) or an anisotropic reflectance factor defined as follows (Taylor and Stowe 1984):

$$f_\lambda(\theta_0, \theta, \phi) = \frac{\pi I_\lambda(\theta_0, \theta, \phi)}{F_\lambda}, \qquad (11)$$

where $I_\lambda(\theta_0, \theta, \phi)$ is the radiance backscattered in a direction specified by the viewing zenith angle θ and the relative azimuth angle ϕ between the viewing direction and the solar beam; θ_0 is the solar zenith angle; and F_λ is the upward irradiance at the level where $I_\lambda(\theta_0, \theta, \phi)$ is measured, which in this case is the top of the atmosphere (TOA). By definition the anisotropic reflectance factor represents the extent to which the backscattered radiation field departs from isotropy. Its value is unity when the radiation field is isotropic. Note that the anisotropic reflectance factor f multiplied by the surface albedo over π equals the BRDF (i.e., BRDF = (A_g/π) f, where A_g is the surface albedo).

Figure 1 shows the patterns of the bidirectional anisotropy factor in AVHRR channel 1 computed by the radiative transfer model described above for (a) a bare snow surface (no atmosphere), (b) at the TOA over a snow surface under clear-sky conditions (no clouds and/or aerosols), and (c) at the TOA over a snow surface under cloud-free conditions in the presence of haze. The solar zenith angle is taken to be 70°. Negative viewing angles refer to the antisolar side. For a bare snow surface (Fig. 1a) the values of the contours range from 0.22 to 5.50, far from unity, indicating that the radiation reflected by the snow surface is highly anisotropic in the visible band, which is consistent with observations. In Fig. 1b the range is smaller than that for the bare snow surface. Thus, the TOA radiation field under clear-sky conditions in the absence of haze is less anisotropic than the BRDF for the bare snow surface (no atmosphere). But the minimum and the maximum values range from 0.70 to 3.11, still far from unity. Figure 1c shows that the addition of haze slightly reduces the degree of anisotropy in the TOA radiation field over a snow surface so that the anisotropy factor is more uniform, ranging from 0.73 to 2.78.

4. Clear-sky retrieval of surface properties

Proper treatment of the bidirectional reflectance is important for the correct interpretation of satellite data because satellite sensors with narrow fields of view measure reflected radiances within a narrow cone of solid angle. The anisotropy of the reflected radiation is particularly significant for low solar elevations, which at high latitudes occur most of the time throughout the year. Previous investigators have developed techniques for retrieving surface albedo and solar irradiances from satellite-measured radiances (e.g., Saunders 1990; Stuhlmann and Bauer 1990; Pinker and Laszlo 1992; de Abreu et al. 1994). Most methods rely on the use of an empirical anisotropic correction factor to account for the bidirectional reflectance, while the underlying surface is assumed to be a Lambertian reflector. The anisotropic correction is usually done by multiplying the TOA albedo (obtained by assuming that the TOA backscattered radiation is isotropic) with an empirical anisotropic correction factor, which is based on results from the Earth Radiation Budget Experiment (ERBE) studies of anisotropic reflectance over various surfaces (e.g., Taylor and Stowe 1984; Suttles et al. 1988). However, ERBE is a broadband instrument so it is commonly assumed that the correction factor is the same in AVHRR channels 1 and 2 (de Abreu et al. 1994). Lubin and Weber (1995) have shown that this is generally not the case.

In this study, we develop an algorithm that is specifically tailored to arctic conditions. The bidirectional reflectance of snow surfaces is included in the coupled radiative transfer model, as opposed to assuming a Lam-

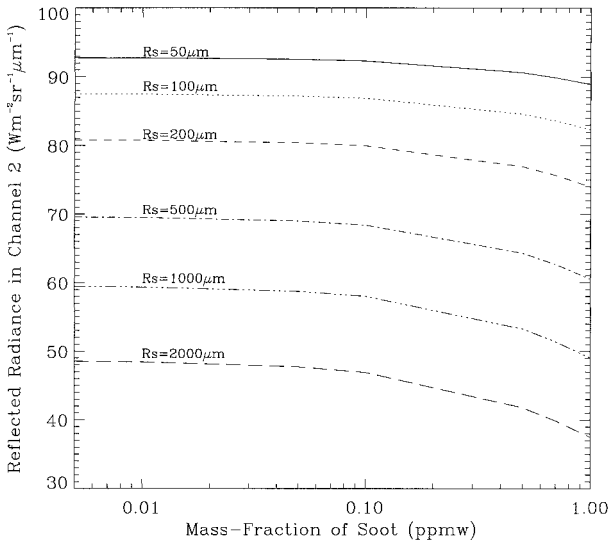

FIG. 3. Simulation of reflected solar radiances in AVHRR channel 2 as a function of the mass fraction of soot and snow grain size with the condition of solar zenith angle $\theta_0 = 60°$, satellite zenith angle $\theta = 10°$, and relative azimuth angle between the sun and the satellite $\phi = 50°$.

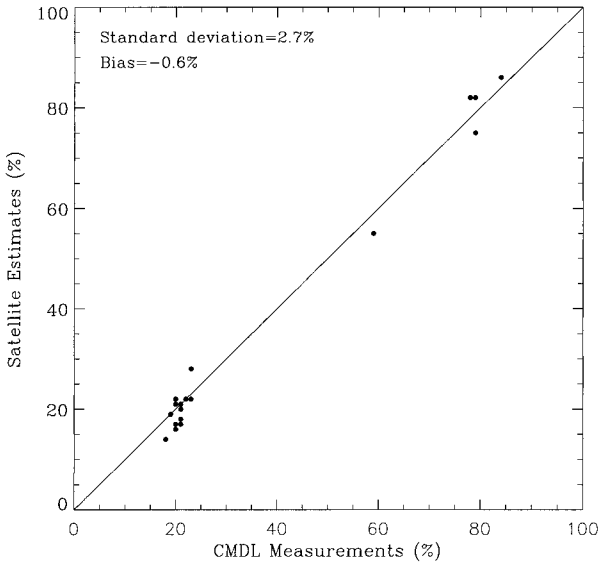

FIG. 4. Scatterplots of satellite estimates vs ground-based CMDL measurements of broadband albedo for all 19 cloud-free cases (tundra and snow).

bertian reflector. Two different procedures are developed depending on the underlying surface type.

a. Retrieval procedures

In the case of tundra, the surface albedo for channels 1 and 2 is given an initial value based on field measurements made by Grenfell and Perovich (1984) at Barrow, Alaska. Then the TOA radiances for channels 1 and 2 are computed separately by the radiative transfer model with the sun-satellite geometry information as input parameters. This process is repeated by adjusting the surface albedo for channels 1 and 2 until the computed radiances match the observed TOA radiances of AVHRR channel 1 and channel 2, respectively. We then compute the broadband surface albedo in the solar region using the following narrowband-to-broadband conversion equation suggested by Key (1996):

$$\alpha = 0.0034 + 0.34\alpha_1 + 0.57\alpha_2, \qquad (12)$$

where α is the clear-sky broadband surface albedo over snow-free land; α_1 and α_2 are narrowband surface albedo for channels 1 and 2, respectively. Note that Eq. (12) was derived for vegetation rather than tundra. Lacking information on tundra, we use it in this study.

Figures 2 and 3 illustrate the reflected radiance in channels 1 and 2, respectively, as a function of the mass fraction of soot and snow grain size. Figure 3 shows that the TOA radiance in channel 2 is generally not sensitive to the amount of soot embedded in the snow when the mass fraction of soot is less than 1 ppmw. According to Clarke and Noone (1985), the mass fraction of soot was estimated to range from 0.01 to 0.06 ppmw for Arctic snow/ice based on observations. Therefore, in the case of snow, the first step is to adjust the snow grain size until the computed TOA radiance in channel 2 agrees with the measured radiance. In the second step after the grain size is determined, the mass fraction of soot in the snow will be estimated by the same procedure using the radiance of channel 1. Using the derived snow grain size and the mass fraction of soot as input, we can compute the wavelength-dependent as well as the broadband (by integration) upward and downward solar irradiances at the air–snow interface from the radiative transfer model. The ratio of upward to downward broadband solar irradiance yields the broadband albedo of snow. Note that the mass fraction of soot is usually higher during the snow melting season and that the independence of the channel 2 radiance of the mass fraction of soot is not valid (see Fig. 3). To retrieve snow grain size and mass fraction of soot, the above procedures for channel 1 and channel 2 should be repeated until the computed radiances in channels 1 and 2 agree with the satellite measurements. This procedure can also be applied to snow surfaces in midlatitudes where the amount of soot embedded in snow is sometimes higher than in the Arctic.

b. Retrieval results

The algorithms described above are applied to clear AVHRR pixels selected for Barrow, Alaska, from April to August of 1992. Figure 4 compares the retrieved albedo values (vertical axes) with field measurements (horizontal axes) for a total of 19 cloud-free cases. In this figure, a group of 14 data points has an albedo close to 20%. Another group of four has a much higher albedo

of about 80%. Obviously the group with low surface albedo pertains to summer conditions when the underlying surface is snow-free tundra, while the high albedo values pertain to winter when the underlying surface is covered by snow. The data point with an intermediate value of albedo (about 60%) comes from a time when snow is in the process of melting.

As we can see from Fig. 4, the bias is very small (−0.6%) while there is some scatter between the retrieval results and the surface measurements, the root-mean-square (rms) deviation being 2.7%. The scatter may be partly due to the Lambertian approximation for tundra surfaces, and the narrowband-to-broadband conversion [Eq. (12)] for tundra surfaces. As mentioned above, Eq. (12) was derived for vegetation, not specifically for tundra. In addition, part of the scatter is probably due to the different fields of view of satellite sensors and pyranometers as well as atmospheric variability, and uncertainty in pyranometer measurements and satellite navigation.

c. Effect of bidirectional reflectance of snow

In this study we also test the validity of the Lambertian assumption over snow. Treating snow as a Lambertian surface, we use the same retrieval procedure as for tundra to determine the narrowband albedo of snow in channel 1 and channel 2. The broadband albedo of a snow surface can be determined by the conversion

$$\alpha = 0.04228 + 0.661\alpha_1 + 0.208\alpha_2, \qquad (13)$$

suggested by Key (1996) based on measurements made on the Greenland ice sheet.

Figure 5 has the same format as Fig. 4 but focuses on only the 5 out of the 19 cases for which the underlying surface is snow covered. The solid points represent results for a snow surface with bidirectional reflectance properties, while the circles display similar results based on the Lambertian assumption. Figure 5 shows that the retrieval results become worse when we use the Lambertian assumption. The bias for a snow surface with bidirectional reflectances is very small for albedo (0.1%). The albedo bias increases dramatically when the Lambertian (isotropic) assumption is invoked, being (−9.0%). It is also evident from Fig. 5 that the rms deviation for the inferred albedo obtained when the surface is treated properly as a bidirectional reflector (6.1%) is much smaller than when it is taken to be a Lambertian reflector (13.0%). In the cases shown in Fig. 5, the surface albedo is underestimated by as much as 30% when we use the isotropic assumption compared to a snow surface with bidirectional reflectance properties. Knowing the viewing geometry for these cases, we can estimate anisotropic reflectance factors. By inspecting Fig. 1 we find that they are all less than unity, which is most likely the reason for the underestimation of the surface albedo resulting from the Lambertian assumption. The scatter in Fig. 5 may be partly due to the fact that Eq. (12) is based on data from the Greenland ice sheet that may be inappropriate for conditions at Barrow, Alaska.

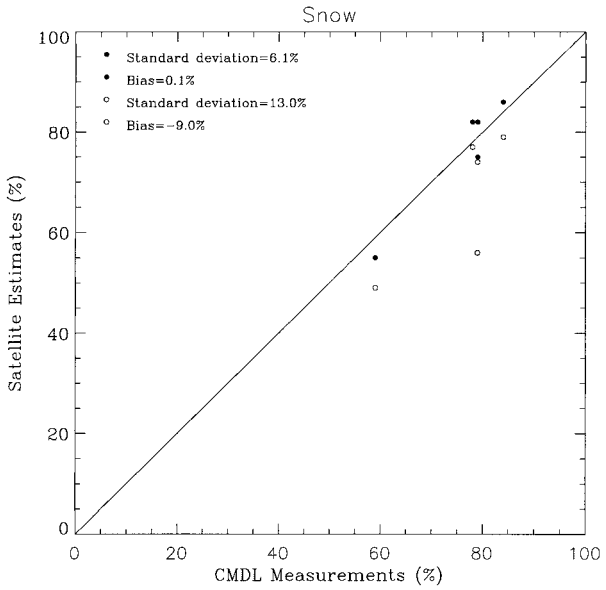

FIG. 5. Scatterplots of satellite estimates of albedo using a computed bidirectional reflectance function (solid point) and with Lambertian assumption (circle) vs CMDL field measurements of broadband albedo.

5. Cloud remote sensing

a. Principles of cloud remote sensing

1) WATER CLOUD OVER OCEAN OR TUNDRA

Figure 6 (similar to Fig. 1 of Nakajima and Nakajima 1995) shows that the reflected solar radiance in channel 1 depends primarily on the cloud optical depth (upper panel), while the reflected solar radiance in channel 3 depends primarily on the effective radius (lower panel) when the cloud is sufficiently thick ($\tau > 3$). This can be explained by the fact that the magnitude of the imaginary index of refraction of liquid water in channel 3 (about 10^{-3}) is much larger than that in channel 1 (about 10^{-9}). This results in much stronger liquid water absorption in channel 3 than in channel 1. Therefore, the reflected radiance of channel 3 is sensitive to cloud droplet size and is approximately inversely proportional to droplet radius.

In channel 3, however, the thermal radiation emitted by ground and cloud layers can be comparable to the reflected solar radiance for typical cloud particle sizes encountered. Figure 7 shows simulated radiances in channel 3 as a function of optical depth in the case of 1) no thermal radiation, 2) with ground thermal radiation, 3) with cloud thermal radiation, and 4) with both ground and cloud thermal radiation. This figure (which is similar to Fig. 4 of Nakajima and Nakajima 1995)

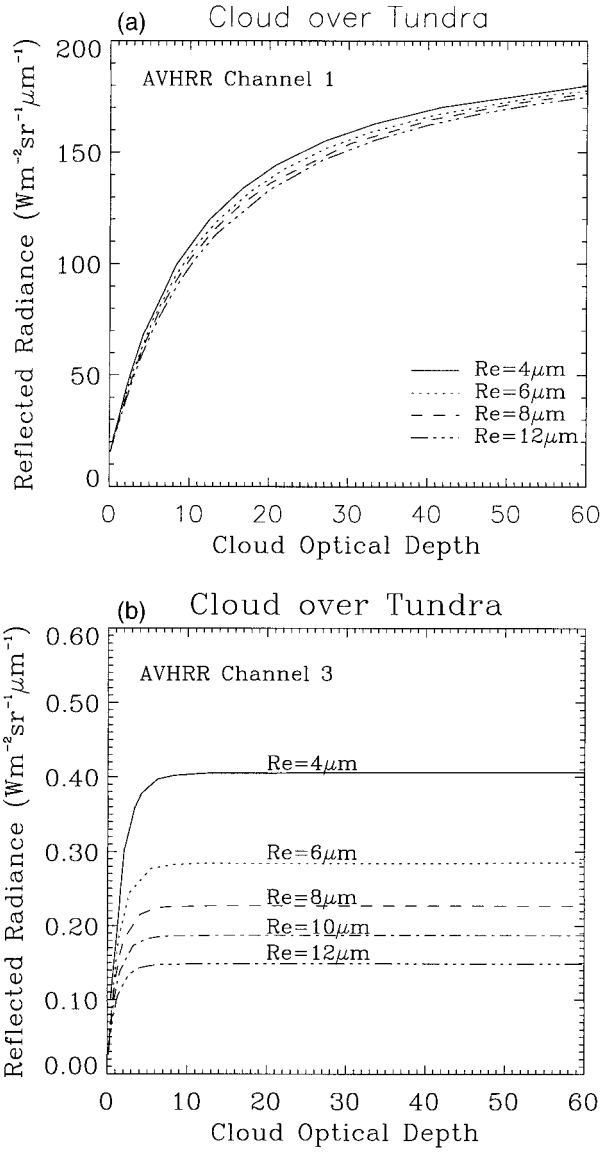

FIG. 6. Reflected radiance for (a) AVHRR channel 1, and (b) AVHRR channel 3 for various effective radii as a function of cloud optical depth. Calculations are for the azimuth angle $\phi = 50°$, satellite zenith angle $\theta = 10°$, and solar zenith angle $\theta_0 = 60°$, respectively. Lambertian visible surface albedo is 0.1.

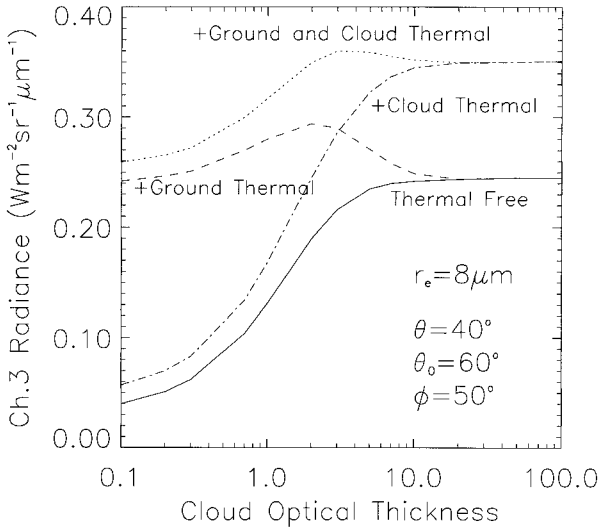

FIG. 7. Simulated radiances of AVHRR channel 3 as a function of cloud optical depth in the case of 1) no thermal radiation (i.e., reflected sunlight only), 2) with ground thermal radiation, 3) with cloud thermal radiation, and 4) with both ground and cloud thermal radiation, for a surface temperature $T_g = 288.2$ K, cloud-top temperature $T_c = 275.2$ K, and surface albedo $A_g = 0.0$.

illustrates that the contribution of ground thermal radiation is large when cloud optical depth is less than 10 and that the contribution of cloud thermal radiation is obvious when optical depth is greater than 2. The effect of ground thermal radiation together with cloud thermal radiation is profound especially in the case of a thin cloud (optical depth less than 1). Therefore, we have to take into account the thermal component by including the thermal channel at 11.0 μm (channel 4) for inferring cloud-top temperature, as discussed below.

The brightness temperature of AVHRR channel 4 as a function of cloud optical depth is plotted in Fig. 8 for several cloud-top temperatures, effective radii, and ground temperatures. Channel 4 brightness temperature converges to the ground temperature when the cloud is thin and τ is close to zero since the ground surface can be approximated as a blackbody in channel 4. The brightness temperature converges to the cloud-top temperature when the cloud is thick since the emissivity of a thick cloud is nearly equal to 1. This property makes channel 4 an ideal channel for retrieval of cloud-top temperature. For a cloud containing large droplets (effective radius greater than 10 μm), the channel 4 brightness temperature is insensitive to cloud particle size. When cloud optical depth is greater than 5, the channel 4 brightness temperature is insensitive to ground temperature.

In summary, through measurements of AVHRR channels 1, 3, and 4 we can retrieve cloud optical depth, effective radius, and cloud-top temperature of water clouds over ocean and tundra.

2) WATER CLOUD OVER SNOW OR ICE

For clouds over highly reflecting surfaces like snow and ice, the radiance in AVHRR channel 1 is no longer primarily a function of cloud optical depth. Figure 9 shows that ground reflectance contributes significantly to the radiance in AVHRR channel 1 and that the reflected radiation in channel 1 is insensitive to cloud optical depth when the surface albedo is large for reasons explained previously. However, the channel 2 radiance depends primarily on cloud optical thickness for cloud over snow/ice, as shown in Fig. 10 (upper panel). The lower panel indicates that the reflected radiance in

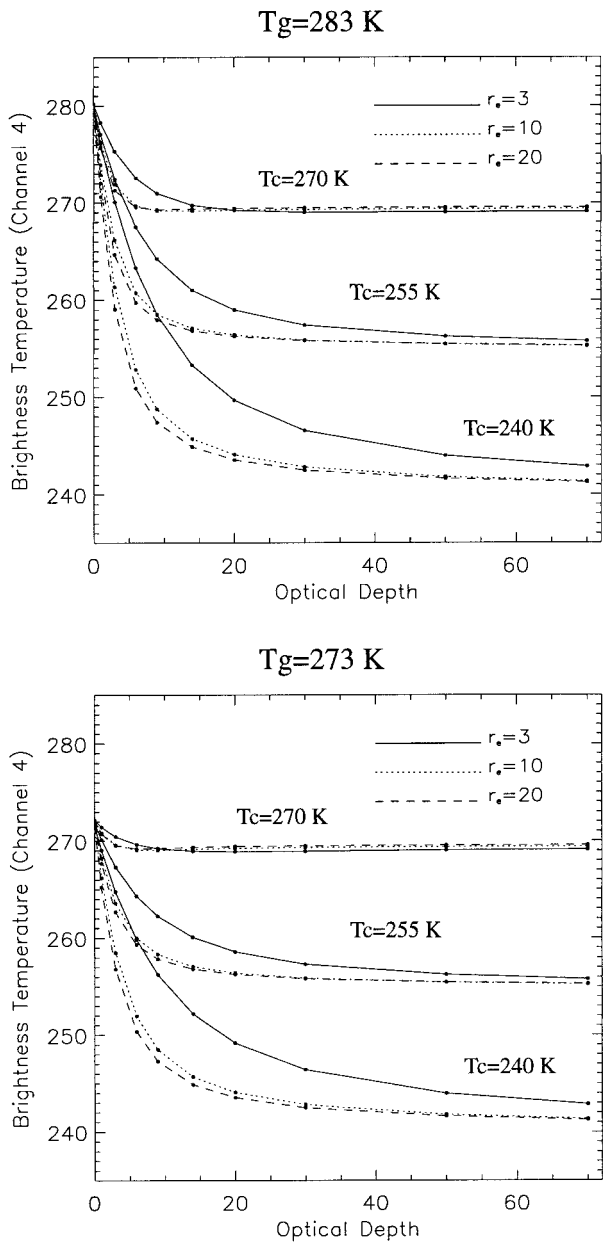

FIG. 8. Brightness temperature of AVHRR channel 4 for for several values of cloud-top temperature and effective radius as a function of cloud optical depth for a surface temperature of 273 K (lower panel) and 283 K (upper panel).

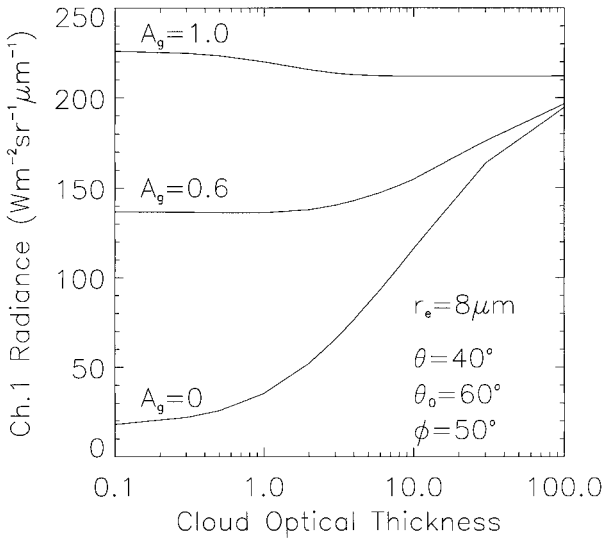

FIG. 9. Simulated radiances of AVHRR channel 1 as a function of cloud optical depth for several values of surface albedo A_g. The middle and lower lines give results for the Lambertian assumption, while the upper line (for $A_g = 1$) is for a non-Lambertian snow surface resulting from coupling the atmosphere to the snowpack.

channel 3 is primarily a function of effective radius for cloud over snow or ice, which is similar to the case of cloud over ocean and tundra. This is because the albedo of a snow surface drops sharply at near-infrared wavelengths. Similarly, the thermal radiation in channel 3 can be estimated by using the thermal channel at 11.0 μm (channel 4) for inferring cloud-top temperature. The middle and lower lines in Fig. 9 are obtained from adopting a Lambertian surface with fixed albedo. The upper line shows the radiance for a snow grain size of 50 μm (which yields albedo A_g close to 1) when the underlying snowpack is coupled to the atmosphere. While the Lambertian assumption leads to a decrease in reflected radiance with increasing cloud optical depth, the inclusion of a snow BRDF (upper line) leads to a reflectance that is nearly constant with optical depth. This is contrary to the assertions made in the literature (Loeb 1997) that at low solar elevations, radiative transfer calculations show a tendency for nadir reflectance to decrease at visible wavelengths when a cloud layer (regardless of thickness) is inserted above a highly reflecting snow surface. Thus, the Lambertian assumption can lead to misinterpretations of satellite data over snow.

In summary, through measurements of AVHRR channel 2, 3, and 4 we can retrieve optical depth, effective radius, and cloud-top temperature of water clouds over snow and ice in the Arctic. Key (1999) assumed that snow acts as a Lambertian reflector. He found that multiple solutions occur when the solar zenith angle is large. Figure 11 indicates that accounting for bidirectional reflectance of snow significantly improves the quality of the retrieval algorithm as compared with the Lambertian approximation. Although this figure does not prove that multiple solutions can always be avoided by including the underlying surface as an additional layer, it provides an encouraging indication that such might be the case.

b. Description of retrieval algorithm

The discrete-ordinate multiple scattering solutions are computationally too expensive to use directly on individual pixels, so they are instead used to generate lookup tables for a given satellite image and satellite viewing

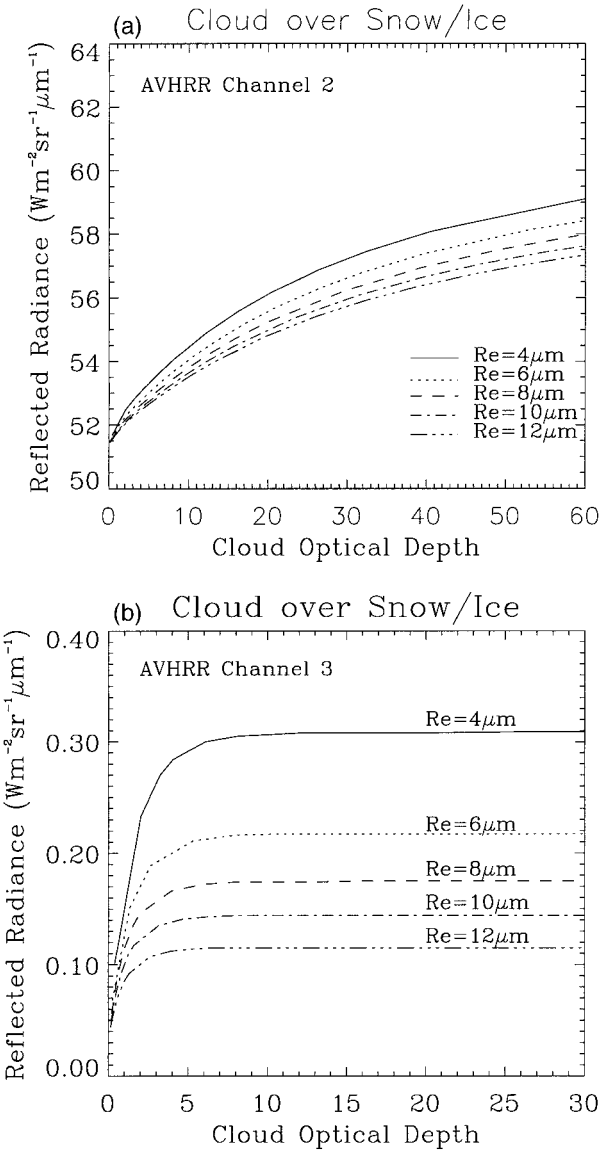

FIG. 10. Reflected radiance for (a) AVHRR channel 2, and (b) AVHRR channel 3 for several values of effective radius as a function of cloud optical depth. Calculations are for the azimuth angle $\phi = 50°$, satellite zenith angle $\theta = 10°$, and solar zenith angle $\theta_0 = 70°$, respectively. Snow grain size is assumed to be 100 μm, which corresponds to a surface visible albedo of 0.95.

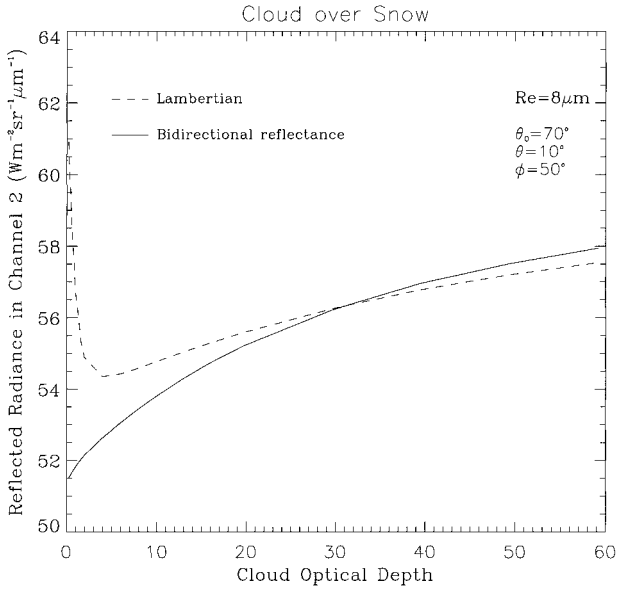

FIG. 11. Reflected radiance in AVHRR channel 2 as a function of cloud optical depth. Calculations are for the azimuth angle $\theta = 50°$, satellite zenith angle $\theta = 10°$, and solar zenith angle $\theta_0 = 70°$, respectively. Snow grain size is assumed to be 100 μm, which corresponds to a surface albedo of 0.87 in AVHRR channel 2. The solid line represents the calculations from the model that account for bidirectional reflectance of snow, and the dotted line represents the calculations from the model based on a Lambertian reflector for snow. Cloud effective radius is 8 μm.

geometry. Below we describe two different retrieval procedures designed for two different surface types: ocean/tundra and snow/ice.

1) WATER CLOUD OVER OCEAN OR TUNDRA

To reduce the computational burden, we must determine to which parameters the reflected radiation in the AVHRR channels is most sensitive. According to Han et al. (1994), cloud effective radius is important for the solar reflectance in channel 3 only, and cloud-top temperature (T_c) is important for thermal radiation in channel 3 and channel 4, but not for solar reflectance in channel 1 and channel 3. The effect of T_c on channel 1 and channel 3 solar reflectance is determined by gaseous absorption and Rayleigh scattering above the cloud top since a change in cloud-top temperature implies a change in cloud-top height and, hence, a change in the amount of gas above the cloud top. In channel 1, variation of the gas amount above the cloud-top changes the Rayleigh scattering contribution slightly. In channel 3 the variation of water vapor amount changes the solar radiation absorbed by water vapor above the cloud top. Only the air above the cloud absorbs or scatters radiation observed by satellites because water clouds have large albedo at visible wavelengths and are strong absorbers at 3.7 μm, so that not much sunlight can reach the atmosphere below the cloud. Cloud optical depth has a significant impact on the solar reflectance in channel 1 as well as channel 3, when the cloud is thin, as illustrated in Fig. 6. The thermal component of channel 3 is also sensitive to cloud optical depth, and channel 4 radiance is sensitive to τ when the cloud is thin, as demonstrated in Fig. 8. Since ground reflectance significantly contributes to the radiance measured by satellites in channel 1 (shown in Fig. 9), accurate estimation of surface albedo for channel 1 is needed. Ground temperature has little effect on channel 4 brightness temperature when the cloud is thick and can be determined by channel 4

brightness temperature from a clear-sky pixel (shown in Fig. 8).

Four lookup tables are generated for retrieval of cloud properties over tundra. They are (I) channel 1 radiance as a function of surface albedo for clear sky; (II) channel 1 radiance as a function of cloud optical depth and surface albedo; (III) channel 3 radiance as a function of cloud optical depth, effective radius, cloud-top temperature, and ground temperature; and (IV) channel 4 radiance as a function of cloud optical depth, effective radius, cloud-top temperature, and ground temperature. Dependencies of the radiances on solar zenith angle, satellite viewing angle, and relative azimuth angle between the sun and the satellite are also taken into account in all the tables. In the lookup tables the visible cloud optical depth was discretized as follows: 1.0, 3.0, 6.0, 9.0, 14.0, 20.0, 30.0, 50.0, 70.0, and the discretization of the cloud effective radius (in μm) was 1.0, 3.0, 5.0, 6.5, 8.0, 10.0, 12.0, 17.0, 22.0, 30.0.

In step 1, a clear-sky image is selected to determine the surface albedo A_g of the tundra surface from lookup table I and the observed channel 1 radiance $R_{\text{sat,ch1}}$. For ocean surfaces, the albedo remains nearly constant when the solar zenith angle is less than 60°. Thus it is fixed to be 0.06, which is also used for cloud retrieval at mid- and low-latitudes (Platnick and Valero 1995). In step 2, we take the surface albedo under cloudy skies to be the same as when the clear-sky image was taken. The surface albedo obtained in step 1 together with channel 1 radiance in the cloudy image is then used to compute cloud optical depth τ from lookup table II. In step 3, a value for cloud effective radius r_e is obtained from lookup table III using the observed channel 3 radiance $R_{\text{sat,ch3}}$, in conjunction with the cloud optical depth obtained in step 2, with an initial value of cloud-top temperature T_c selected to be equal to the brightness temperature in channel 4, and the ground temperature T_g. The ground temperature T_g is determined from the channel 4 brightness temperature at nearby clear pixels.

In step 4, a value for cloud-top temperature T_c' is obtained from lookup table IV using observed channel 4 radiance $R_{\text{sat,ch4}}$ as input in conjunction with the cloud optical depth obtained from step 2 and the effective radius obtained in step 3. If the difference between this improved estimate for cloud-top temperature and the initial value $\Delta T_c = |T_c - T_c'|$ is large, we return to step 2 with the improved T_c' as the new initial value of cloud-top temperature to get a new set of cloud effective radius and cloud-top temperature. The iteration ends when ΔT_c is less than 0.1 K. The three parameters τ, r_e, and T_c are then obtained through steps 1 and 2, and the iteration of steps 3 and 4. Generally, the iteration converges after two or three rounds.

2) WATER CLOUD OVER SNOW OR ICE

As in the case of cloud over tundra, four lookup tables are prepared for the retrieval of cloud parameters over snow or ice. They are (I) channel 2 radiance as a function of snow grain size under clear sky; (II) channel 2 radiance as a function of cloud optical depth, effective radius, and snow grain size; (III) channel 3 radiance as a function of cloud optical depth, effective radius, cloud-top temperature, and ground temperature; and (IV) channel 4 radiance as a function of cloud optical depth, effective radius, cloud-top and ground temperatures. The dependencies of the radiances in channels 2, 3, and 4 on solar zenith angle, satellite viewing angle, and relative azimuth angle between the sun and satellites are also taken into account in these lookup tables.

As the first step, the grain size of the underlying snow surface is retrieved from a clear-sky channel 2 image and lookup table I. In step 2, an estimated value of cloud optical depth is obtained from lookup table II using the observed cloudy-sky channel 2 radiance and an initial value of cloud effective radius as input. Note that this may not be the ultimate retrieval of optical depth. In step 3, an estimated value of cloud effective radius is obtained from lookup table III using the observed channel 3 radiance as input in conjunction with the cloud optical depth estimated in step 2, an initial value of cloud-top temperature (brightness temperature in channel 4), and the ground temperature. In step 4, an estimated value of cloud-top temperature is obtained from lookup table IV using the observed channel 4 radiance as input in conjunction with the cloud optical depth estimated in step 2, the effective radius estimated in step 3, and the ground temperature.

If differences between the estimated values and the given initial values are large, we return to step 2 and repeat steps 2, 3, and 4 with the estimated value replacing the initial values. This iteration ends when the differences are small ($\Delta r_e < 0.1$ μm and $\Delta T_c < 0.1$ K). The iteration usually converges after three or four rounds, which is one or two times more than that for cloud over ocean and tundra. A flowchart of the algorithm is provided in Fig. 12.

c. Uncertainty analysis

1) UNCERTAINTY IN THE RETRIEVAL OF OPTICAL DEPTH

Part of the error in the retrieved cloud optical depth comes from the error in the surface albedo. The upper panel of Fig. 13 shows the sensitivity of the retrieved optical depth to the error in surface albedo for cloud over tundra or ocean. Consider a surface albedo $A_g = 0.06$ with an uncertainty of ± 0.04. The retrieved cloud optical depth becomes larger if we use $A_g = 0.10$ instead of $A_g = 0.06$, and the difference between the two values is a function of the cloud optical depth itself. This function is shown by the line above the zero error line. On the other hand, the retrieved cloud optical depth becomes smaller if we use $A_g = 0.02$ instead of $A_g = 0.06$. The difference as a function of τ is represented

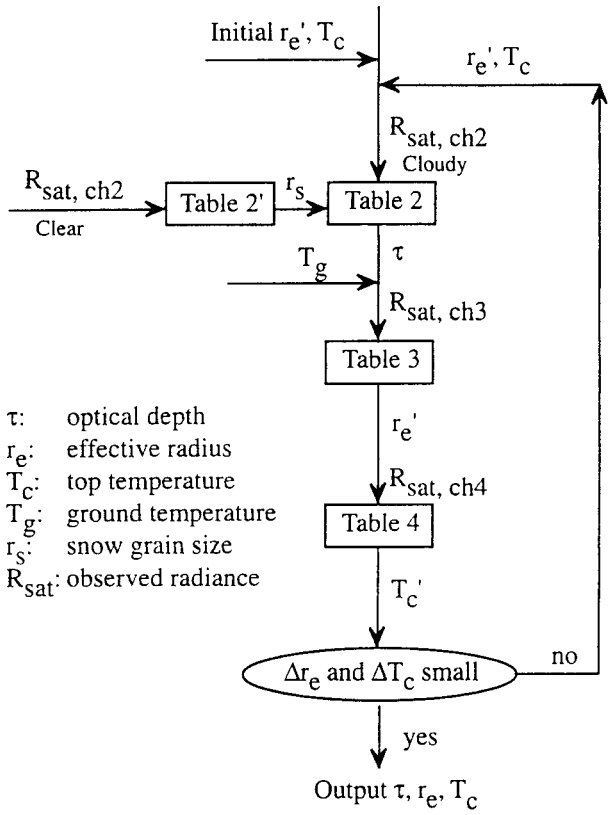

FIG. 12. Flowchart of retrieval algorithm for liquid water cloud over snow and ice.

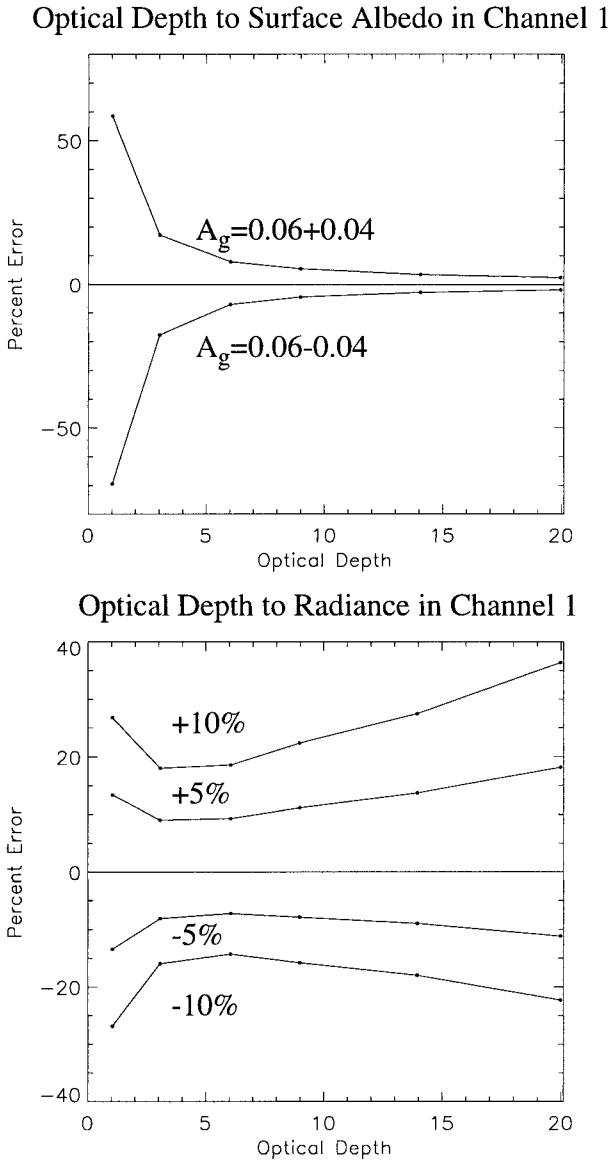

FIG. 13. Error in retrieval of cloud optical depth over ocean and tundra as a function of optical depth for an uncertainty in surface albedo of 0.06 ±0.04 (upper panel) and a ±5% or ±10% error in measured AVHRR channel 1 cloud radiance (lower panel).

by the other line in the upper panel of Fig. 13. The plot shows that the resulting error in the cloud optical depth is small (below 20%) when $\tau > 3$. However, the relative error can be very large when $\tau < 3$; for example, it is 60%–70% when $\tau = 1$.

The major error source for the retrieval of optical depth stems from uncertainties in the observed radiances. The lower panel of Fig. 13 shows the sensitivity of the retrieved cloud optical depth to uncertainties in channel 1 radiance for cloud over tundra or ocean. Suppose channel 1 radiance is 5% too large. The resulting error in the cloud optical depth incurred by this 5% error in channel 1 radiance is a function of the cloud optical depth itself, as indicated by one of the lines in the lower panel of Fig. 13. The other three lines in the plot have similar meanings. When cloud optical depth is larger than 2, a 5% error in channel 1 radiance may result in an error of around 10% in the optical depth. When the cloud is very thin ($\tau < 2$), the error can be quite large.

For cloud over snow or ice, the sensitivity of the retrieved optical depth to the snow grain size and channel 2 radiance is shown in Fig. 14. The upper panel of Fig. 14 shows variations in the retrieved τ for a variation of 100 μm in the snow grain radius as a function of τ itself. The larger the optical depth, the smaller is the resulting variation. When $\tau > 3$, the variation is below 20%. The error in retrieved optical depth can be very large when the optical depth is small ($\tau < 3$). The lower panel of Fig. 14 shows the resulting error in the cloud optical depth for a given error in channel 2 radiance. When $\tau > 3$, the error in optical depth is generally less than 40% for a 4% error in channel 2 radiance. The deviation between Lambertian and non-Lambertian surface types is larger than 3% for optical depths less than 5–6 (see Fig. 11). According to Fig. 14b, if we assume a typical radiometric uncertainty of 3%, then significant deviations between the two surface types occur for cloud optical depths less than 5–6. Thus, accounting for the

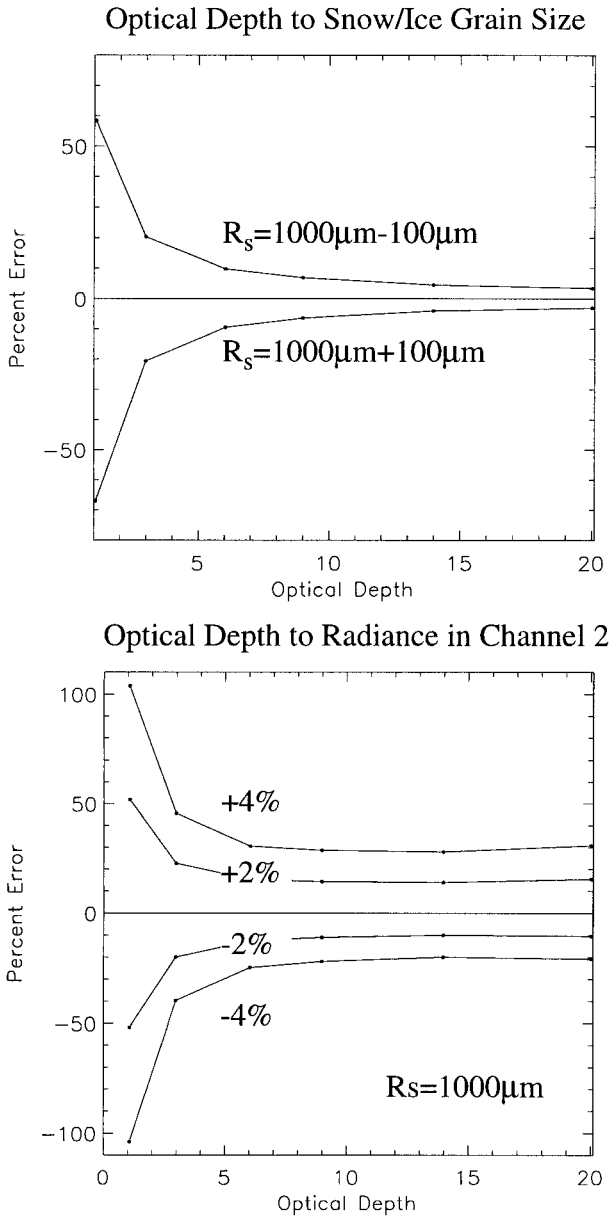

FIG. 14. Error in retrieval of cloud optical depth over snow and ice as a function of optical depth for an uncertainty in snow/ice grain size of 1000 ± 100 μm (upper panel), and a ±2% and ±4% error in measured AVHRR channel 2 cloud radiance (lower panel).

BRDF of snow will improve cloud optical depth retrieval for thin clouds with optical depths between 3 and 6, if we use a typical radiometric uncertainty of 3%. Further reduction in retrieval error will require reduction in radiometric uncertainty significantly below the 3% level. As can be seen from Fig. 14b if the radiometric error is larger than 2%, the error can be large (larger than 100% for $\tau < 1$ when the radiometric uncertainty is 4%). Figure 14 also shows that the retrieved cloud optical depth over snow is much more sensitive to cloud-top radiance than the corresponding retrieval over ocean or tundra.

2) UNCERTAINTY IN THE RETRIEVAL OF EFFECTIVE RADIUS

Surface reflectance has little effect on the retrieval of cloud effective radius because snow, ocean, and tundra all have very low albedo in channel 3. Uncertainties in channel 3 radiance are the primary source of uncertainty in the retrieved cloud effective radius. Since the algorithms for cloud retrieved over tundra/ocean and over snow/ice both use channel 3 radiance and the same principle to retrieve the effective radius, uncertainties in the retrieved effective radii are expected to be similar. Through model calculations we find that a ±10% error of the channel 3 radiance may result in an error of around ∓10% on the retrieved effective radius when the effective radius is larger than 3 μm for optically thick clouds ($\tau > 6$). When the effective radius is smaller than 3, the error of the retrieved value can be very large. There exist other error sources in the retrieved cloud effective radius, as discussed by Han et al. (1994). They include uncertainties caused by horizontal inhomogeneity of the cloud, multilayered cloud structure, cirrus, and aerosol contamination and random errors.

The retrieval scheme of cloud-top temperature used in our study is similar to that used in the International Satellite Cloud Climatology Project (ISCCP). Uncertainties in ISCCP-retrieved cloud-top temperature are caused by the treatment of water vapor effects, cloud effects, and the homogeneity of the cloud, as discussed by Han et al. (1994). The uncertainties associated with water vapor effects are small since the amount of water vapor decreases rapidly with altitude, so that even for low-level clouds a small fraction of the water vapor is above the cloud top. Errors caused by the inhomogeneity of the cloud are also small because of the similarity of brightness temperatures of low-level clouds and clear sky, according to Han et al. (1994).

The investigation by Key and Haefliger (1991) indicated that the attenuation of upwelling infrared radiation in the polar atmosphere is small because of the low atmospheric humidity. Either of channels 4 or 5 alone could be used to derive ice surface temperature. Failure to account for atmospheric correction can result in an ice surface temperature underestimate of 1.5–2.1 K in channel 4 and 1.9–3.2 K in channel 5.

In summary, the major error for both optical depth and effective radius comes from the uncertainty in cloud-top radiance, which in turn comes from uncertainties in calibrations of AVHRR sensors and radiative transfer calculations. For thick clouds with large optical depths and $r_e > 3$ μm, the retrieval results have small errors and are reliable. However, the error can be very large for thin clouds when $\tau < 3$ and $r_e < 3$ μm.

d. Testing of the algorithms

To test the physical soundness and demonstrate the utility of our retrieval algorithms, we have analyzed AVHRR images taken over the North Slope of Alaska and compared the results with ground-based measurements at Barrow, Alaska. There are no in situ data of cloud optical depth or effective radius available for testing. However, we approach this problem by testing higher-level parameters, the downwelling solar irradiance at the surface. There are no direct observations of cloud-top temperature. However, we can derive cloud-top temperatures from radiosonde sounding data and compare them with the retrieval results. Finally, there are no measurements of snow grain size available in Barrow to be used in conjunction with the testing of satellite-inferred values. Thus, we compute the albedo for the retrieved grain size using the raditive transfer model for the coupled atmosphere–snowpack system and compare it to the albedo estimated by taking the ratio of up- and downwelling irradiances measured by the CMDL pyranometers. In the future it would be desirable to measure snow grain size in situ (Grenfell et al. 1994) for direct comparison with satellite-inferred values.

For cloud over tundra, Fig. 15 shows satellite-estimated downwelling irradiance versus ground-based CMDL measurements. The irradiance is an integration for the entire solar spectral band. The ground-based observations are made in Barrow, Alaska. The satellite estimates are obtained by using retrieved cloud parameters as input. Therefore, testing of the downwelling irradiance is an indirect validation of the retrieved cloud parameters. Good agreement is found. The rms deviation over the 17 data points is found to be 45.9 W m^{-2}, and the bias is very small at 5.8 W m^{-2}. The deviation is partly due to temporal and spatial mismatch between the satellite and ground observations. Note that the ground observation is hourly averaged.

Figure 16 is similar to Fig. 15 except that it is for cases with clouds over snow. The satellite estimates agree well with the ground observations. The bias over the 12 data points is small, at 5.1 W m^{-2}, about the same magnitude as the cases with clouds over tundra. The rms deviation is larger, at 45.3 W m^{-2}, which is very close to the case of cloud over tundra.

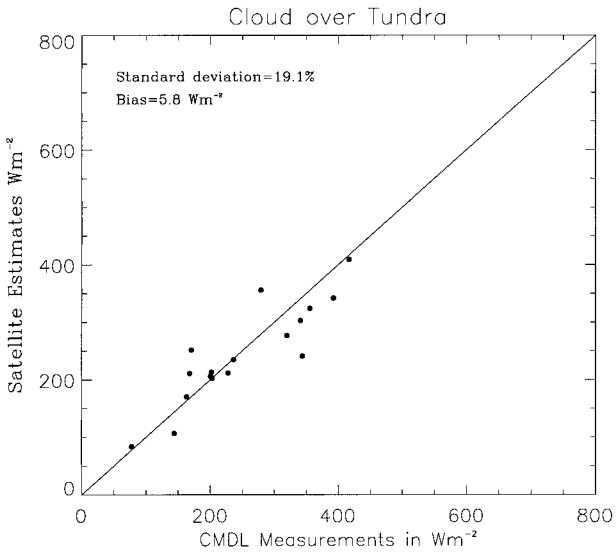

FIG. 15. Scatterplot of satellite irradiance estimates vs ground-based CMDL measurements of solar downwelling irradiance over tundra. The satellite estimates of downwelling solar irradiance at the surface are based on the retrieved cloud parameters.

Radiosonde data are used to validate the cloud-top temperature retrievals. The soundings provide profiles of temperature T and dewpoint temperature T_d, from which the relative humidity is

$$\mathrm{RH} = \frac{\mathrm{svp}(T)}{\mathrm{svp}(T_d)}, \tag{14}$$

where svp is the saturation vapor pressure (List 1968):

$$\mathrm{svp}(T) = 6.1078 \exp\left\{\frac{T[19.846 - T(9.4027 \times 10^{-3} - 3.4442 \times 10^{-5}T)]}{T + 273.0}\right\}. \tag{15}$$

To place the cloud layer using the sounding data, we assume that the cloud top occurs at the bottom of the inversion layer and that the relative humidity is close to 100% in the cloud layers.

Figure 17 summarizes such a validation for nine different cases. The horizontal axis is the cloud-top temperature estimated from sounding profiles, while the vertical axis is the corresponding value retrieved from satellite remote sensing. There is very good agreement between the two. The rms deviation is found to be only 2.4°C, and the bias is 0.03°C. Rossow et al. (1989) found that the error in cloud-top temperature retrieval is about 2°–3°C, which is about the same as our result. It should be mentioned that all nine cases used in Fig. 17 have snow as the underlying surface. Cases with tundra as the underlying surface agree even better with the ground-based sounding results.

Finally, we should note that in the above analysis we have deliberately chosen (by visual inspection of the scenes) cases for which we are reasonably certain that

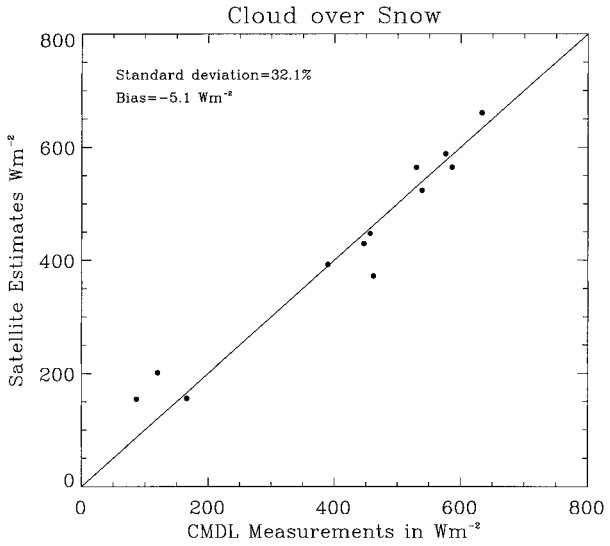

FIG. 16. Same as Fig. 15 but for clouds over snow.

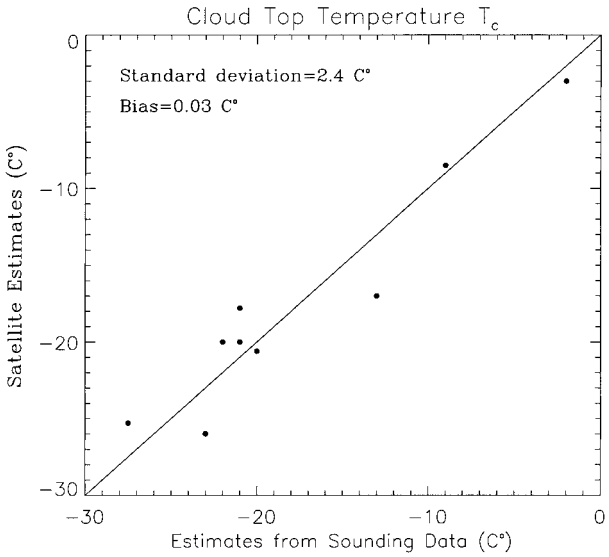

FIG. 17. Scatterplot of satellite estimates of cloud-top temperature vs in situ sounding results.

the ''clear-sky case'' is indeed clear and that the ''cloudy-sky case'' consists of liquid phase clouds. In practice there are several aspects that must be considered from an operational point of view. First one needs a procedure to classify each pixel as clear versus cloudy. Then if the pixel is classified as clear, one must determine the nature of the underlying surface, that is, snow versus tundra, and so on. Our work assumes that these classifications have already been done by others, so they clearly lie outside the scope of the present paper. However, the algorithms discussed in this paper can be used in conjunction with such classification procedures to construct operational cloud–surface retrieval algorithms. Another practical consideration that needs to be addressed from an operational point of view is how to identify ''nearby'' clear pixels in an automated manner. We leave these important operational issues for future consideration and resolution. Lubin and Morrow (1998) have shown that an automated cloud detection and classification technique that uses multispectral and pattern recognition techniques (Ebert 1987) can provide realistic results on an operational basis.

e. Sample retrieval results

To test the basic soundness of the retrieval algorithms, we selected two AVHRR observations that cover scenes over ocean, tundra, and snow. One of the observations is made at 2313 UTC 27 July 1992 under clear-sky conditions. The other observation is made at 0013 UTC 23 July 1992 under mostly overcast conditions. The two observations are about 5 days apart and there is little difference in solar zenith angle between the two images. The clear-sky observation is used to infer surface properties, albedo for tundra, and grain size for snow. We assume that the surface properties are unchanged during the five intervening days so that they can be used as input to retrieve cloud properties from the cloudy-sky observations.

Figure 18 displays the retrieval results for the Chukchi Sea with open ocean as its underlying surface. The solar zenith angle is about 53°. The surface albedo in channel 1 is assumed to be 0.06. From the plot of cloud optical depth in the upper-right panel of Fig. 18, the area appears to be completely overcast, with a fairly thick cloud cover over most of the area with an optical depth between 15 and 50. In a couple of regions, the cloud is extremely thick with an optical depth of about 70 and as large as 80. The cloud droplet size is shown in the upper-left panel of Fig. 18. The droplet radius ranges from 5 to 15 μm in most of the area. Large droplet radius occurs in the lower-right corner of the area where it is close to 18. A weak anticorrelation (Fig. 21b) is found between the cloud optical depth and the droplet size. In the region of large cloud optical depth, the cloud droplet size tends to be small specifically for this case, but the relationship is not strong. The sea surface temperature determined from the channel 4 brightness temperature of a neighboring clear-sky pixel is assumed to be uniform at 277 K. The lower panel of Fig. 18 shows the retrieved cloud-top temperature. The temperature is lower at the cloud top than at the ocean surface, lying generally between 260 to 270 K.

For the Beaufort Sea with snow/ice as the underlying surface, the retrieval results are shown in Fig. 19. The upper-left panel shows the snow grain size. Since it is July when ground temperature is around 0°C, the snow grain size is very large (nearly melting snow), around 1000 μm. The plot for cloud optical depth indicates that the sky is partly cloudy in this area. Note that the black regions are cloud free and the corresponding optical depth is zero. The cloud optical depth is below

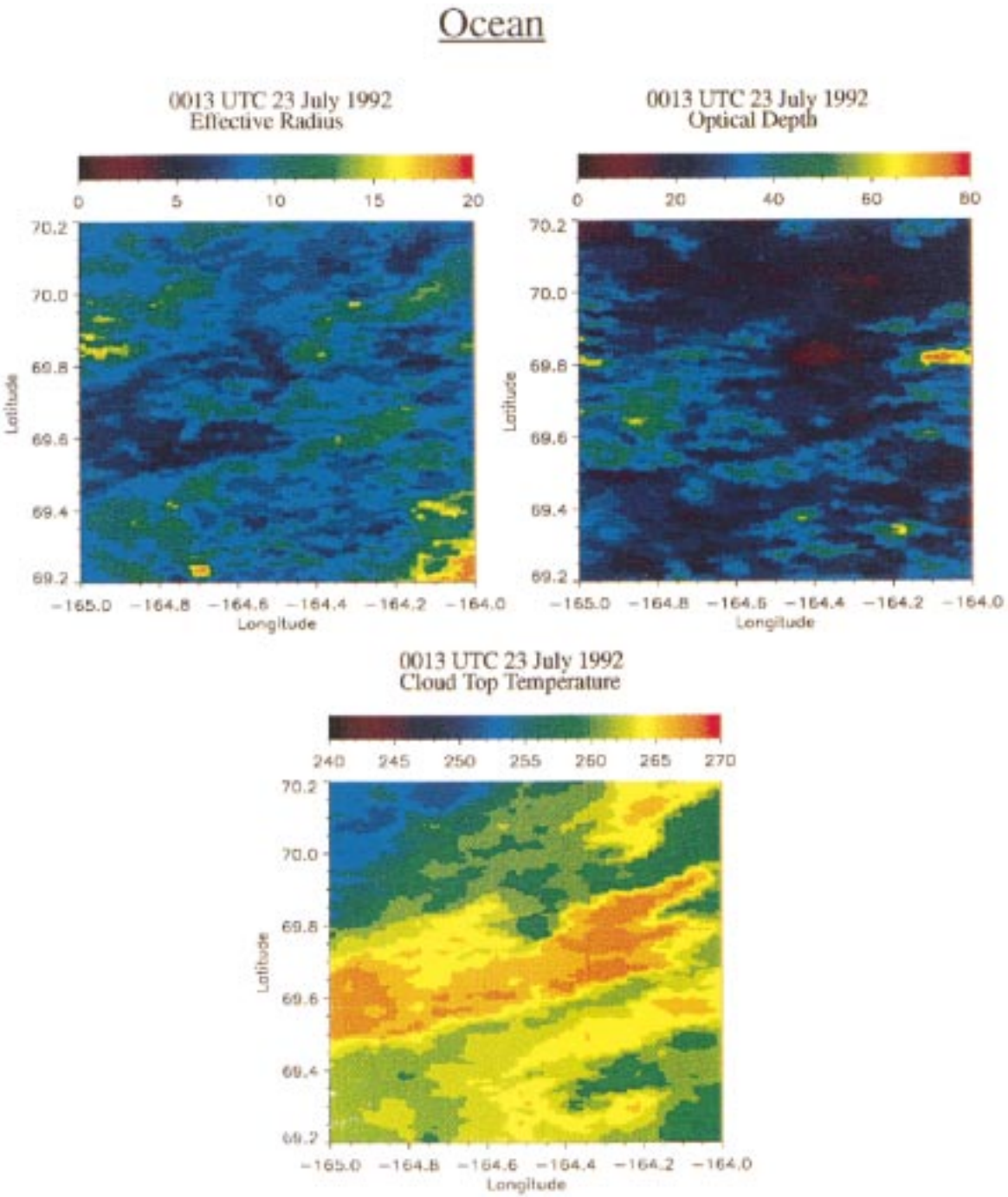

FIG. 18. Derived images of cloud optical depth, effective radius (in μm), and cloud-top temperature (in K) over the Chukchi Sea. The three images are derived from a cloudy image at 0013 UTC 23 Jul 1992. The underlying surface is ocean.

13 in most of the area, while in some other regions it is up to 55. The cloud droplet radius generally lies between 5 and 12 μm. The cloud over the upper-left corner of the area has a large value of droplet radius, around 18 μm. There seems to be no clear correlation between the droplet size and the optical depth. As mentioned previously, we can approximate the surface skin temperature with the TOA brightness temperature because of the dryness of the arctic atmosphere (Key and Haefliger 1991). Then, the ground skin temperature is about 274 K. The retrieved cloud-top temperature is found to be about 267–271 K, slightly lower than the temperature of the ground. In some regions, the cloud top has a temperature slightly higher than the ground

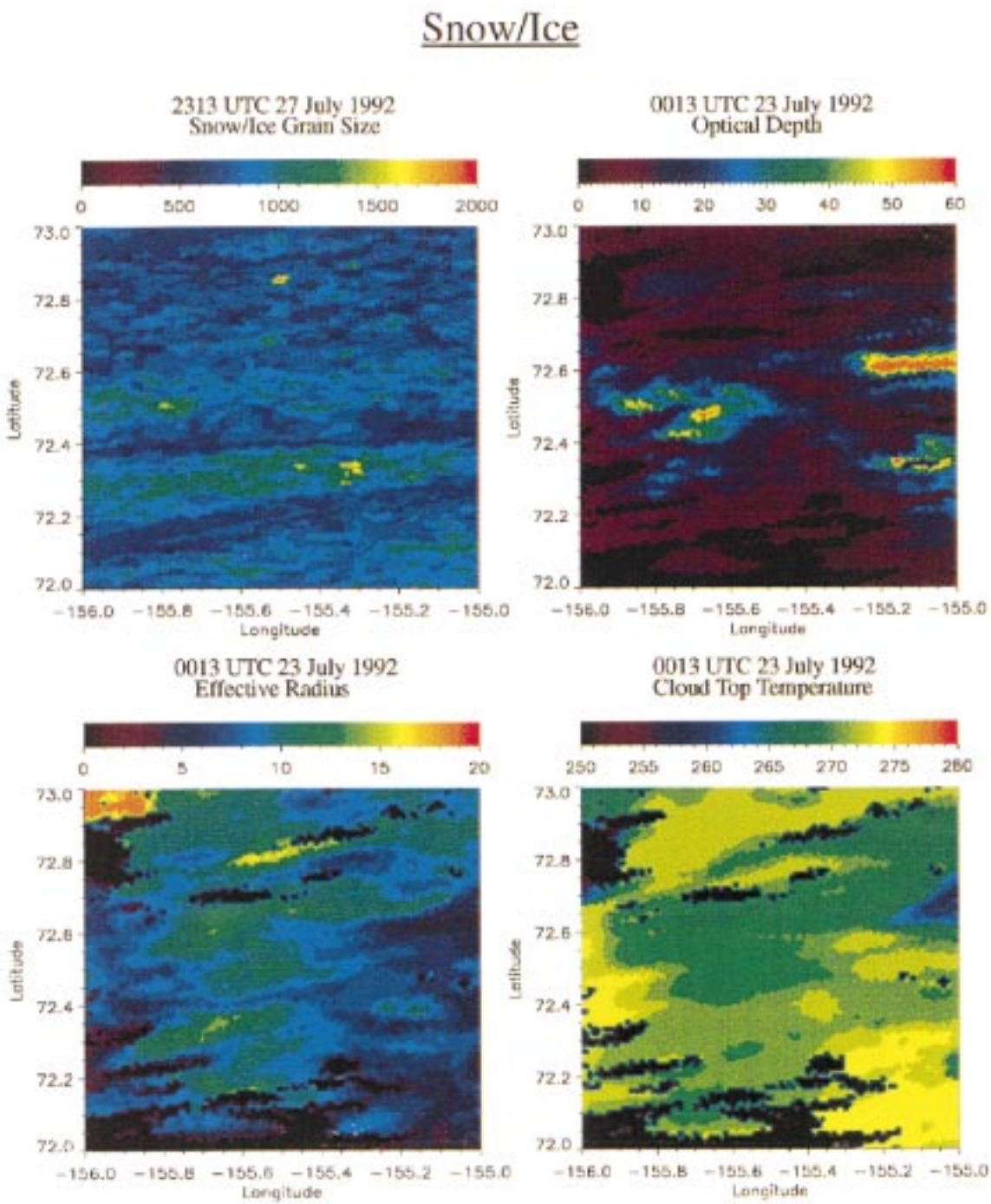

FIG. 19. Derived images of snow grain size in (μm), cloud optical depth, effective radius (in μm), and cloud-top temperature (in K) over the Beaufort Sea. The snow grain size is derived from a clear-sky satellite image at 2313 UTC 27 Jul 1992. The remaining three images are derived from a cloudy images at 0013 UTC 23 Jul 1992. The underlying surface is snow/ice. The black areas in the plots of optical depth, effective radius, and top temperature represent clear sky.

temperature, which indicates a weak temperature inversion over the snow/ice underlying surface even in midsummer.

Figure 20 has the same format as Fig. 19, but it shows retrieval results for the North Slope of Alaska with tundra as its underlying surface. The channel 1 albedo (upper-left panel) is around 0.05 for the tundra surface when the solar zenith angle is 53°. Tundra surface albedo increases with increasing solar zenith angle (Eck et al. 1997). The cloud is thin with optical depth smaller than

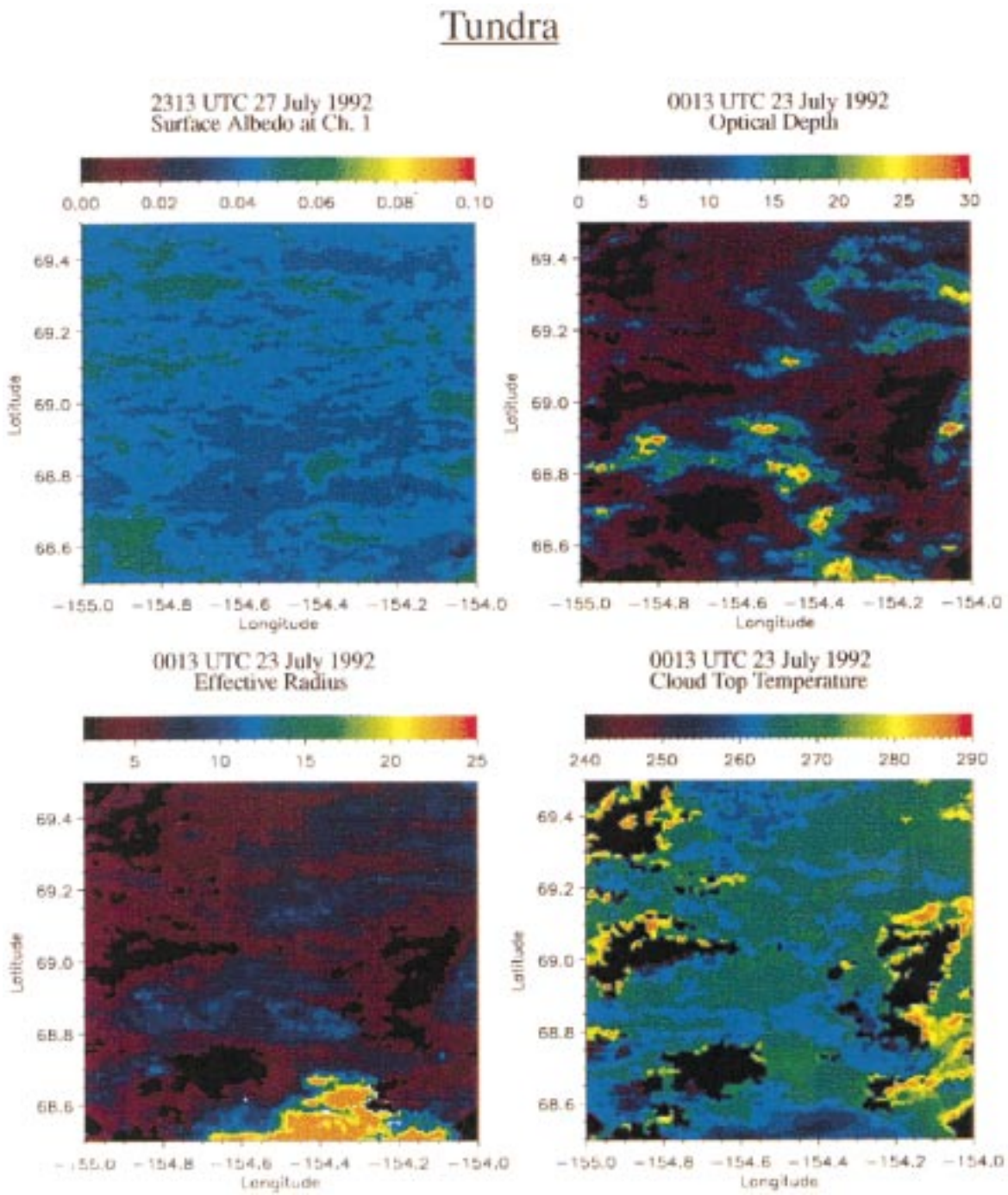

FIG. 20. Same as Fig. 19 except it is for the North Slope of Alaska with tundra as underlying surface and the upper-left panel represents surface albedo in channel 1.

10 in most of the cloudy region. The cloud optical depth and the droplet size show a positive correlation. The tundra skin temperature is relatively high in summer, about 293 K based on the brightness temperature in channel 4 from nearby clear pixels. The retrieved cloud-top temperature is generally around 267 K, similar to that over the ocean. The dark areas indicate clear sky. In the areas neighboring clear sky where cloud is thin, the cloud-top temperature is as high as 290 K, close to the ground skin temperature.

Figure 21 displays the scatterplots of retrieved cloud effective radius versus optical depth for the three areas with different types of underlying surface. Based on a near-global survey of water cloud effective droplet radii,

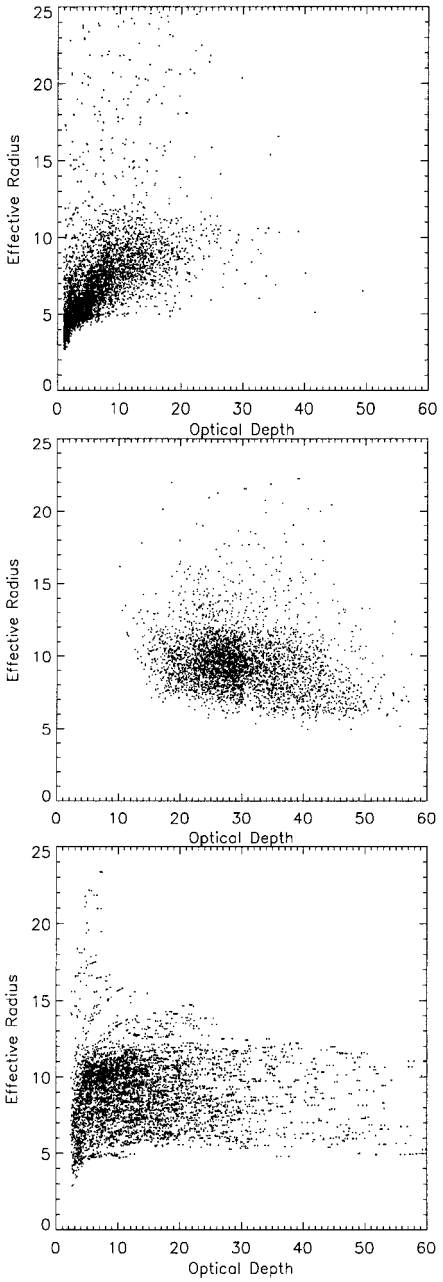

FIG. 21. Scatterplots of retrieved cloud effective radius vs optical depth for areas with ocean (middle), snow (lower), and tundra (upper) as underlying surfaces, respectively.

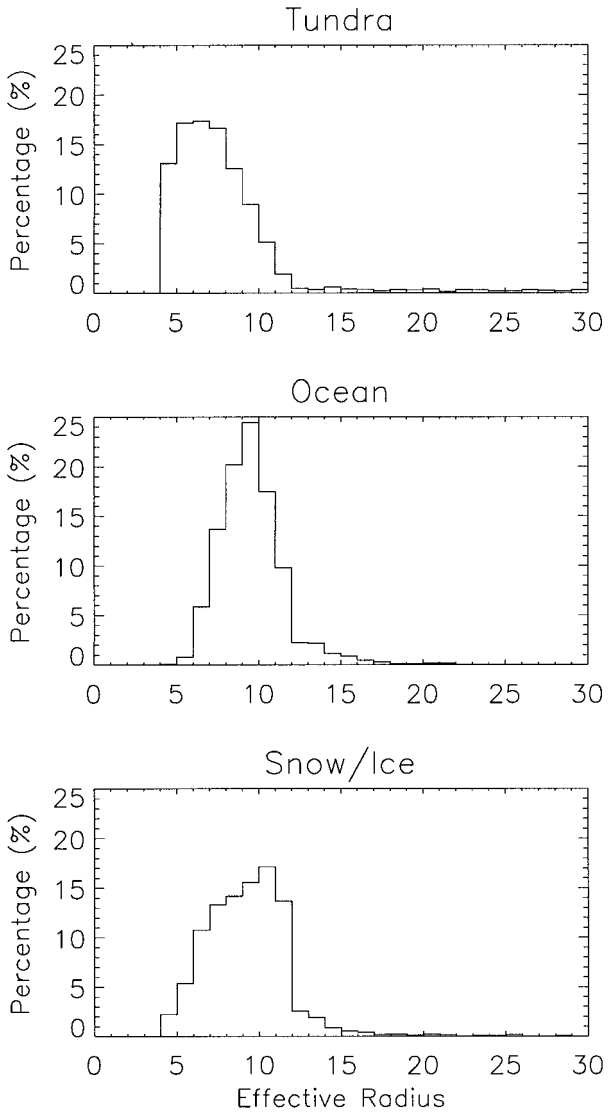

FIG. 22. Frequency distributions of cloud effective radius (in μm) based on the data shown in Figs. 18–20 for tundra, ocean, and snow as underlying surfaces, respectively.

Han et al. (1994) found that cloud droplet radii generally increase with optical thickness for optically thinner clouds ($\tau < 20$) and decrease for optically thicker clouds. This tendency is also evident in Fig. 21. Over ocean, where τ overall is greater than 18, there is a slightly negative correlation between the two quantities. Over tundra, where τ overall is less than 20, there is clearly a positive correlation between the two (Fig. 21a). Over snow/ice τ has a wider range than over ocean and tundra, ranging from 3 to 60. There is a positive correlation between cloud droplet radius and optical thickness when $\tau < 20$ and a very weak negative correlation when $\tau > 20$ over snow/ice. The above relationship between cloud optical depth and effective radius indicates that both cloud optical depth and effective radius are needed to model cloud effects on radiation. Moreover, Curry and Herman (1985) compared aircraft observations to radiative transfer calculations and found that a single-parameter representation, such as liquid water path, did not work because of the variability of cloud particle sizes.

The frequency distribution of effective radius is shown in Fig. 22 for the three different types of underlying surfaces. Over tundra, the effective radius falls

between 4 and 11 μm, with a peak occurrence of 18% at r_e about 7–8 μm. Over the ocean, the droplet size lies mostly between 6 and 12 μm with a peak occurrence of about 25% at r_e about 9–10 μm. Over snow/ice, the effective radius lies generally between 5 and 12 μm, with a peak occurence of 17% at r_e about 10–11 μm. From the three cases shown, we can see that the effective radius for cloud over ocean is generally larger than for cloud over land (tundra), consistent with results for mid- and low latitudes (Han et al. 1994). The retrieved cloud effective radius is generally smaller than in mid- and low latitudes. This may be explained by the low atmospheric humidity in the Arctic. The near-global survey of effective radii in liquid water clouds using ISCCP data by Han et al. (1994) also reveals that the mean cloud droplet radii changes from smaller values in the dry season (January) to larger values in the wet season (July). This behavior is consistent with an association of more frequent rainfall from low clouds with larger droplet sizes (Albrecht 1989) and reduced cloud condensation nuclei (CCN) abundances due to precipitation scavenging (Leaitch et al. 1983).

6. Summary

In this paper, two algorithms are developed to retrieve cloud parameters. The basic features of the algorithms may be summarized as follows.

1) One algorithm is developed for retrieval of cloud properties over dark surfaces like tundra and ocean. This algorithm is suitable for low- and midlatitude areas as well as for high latitudes during summer when the underlying surface is snow/ice free. It relies on the use of AVHRR images in channels 1, 3, and 4 to retrieve cloud optical depth, effective radius, and cloud-top temperature.

2) The other algorithm is designed for retrieval of cloud properties over bright surfaces like snow and ice. It is specifically tailored to arctic regions where large-scale snow/ice cover exists most of the time throughout the year. This algorithm relies on the use of AVHRR images in channels 2, 3, and 4.

3) Bidirectional surface reflection is taken into account in the algorithm designed to retrieve clouds over bright snow/ice surfaces. As illustrated in Fig. 11, the bidirectional reflection function for snow/ice deviates significantly from that of an isotropic Lambert reflector. Accounting for bidirectional reflectance of snow significantly reduces the error in retrieved cloud optical depth as compared with the Lambertian approximation for clouds with optical depths between 3 and 6.

4) The surface albedo is accurately retrieved with both algorithms. For the tundra case, the surface albedo is retrieved from AVHRR channel 1 radiance observed under clear-sky conditions. For bright snow/ice surfaces, the snow grain size is retrieved from AVHRR channel 2 radiance observed under clear-sky conditions.

5) A sensitivity analysis shows that the retrieved cloud properties are reliable for clouds with optical depth $\tau > 3$ and effective radius $r_e > 3$ μm. When $\tau < 3$ or $r_e < 3$ μm, a small error in the observed radiance and surface reflectance may result in large errors in the retrieval results.

6) The retrieval results obtained from the algorithm applicable to bright surfaces are more sensitive to uncertainties in the observed radiance and the radiative transfer model than the corresponding retrievals for dark surfaces.

To test the algorithms, the retrieved cloud parameters are used in the radiative transfer model to compute downwelling irradiance at the surface, and the results are compared with ground-based irradiance measurements obtained at the NOAA/CMDL facility in Barrow, Alaska. The retrieved cloud-top temperature is compared to cloud-top temperature derived from ground-based radiosonde sounding data. These comparisons show the following.

1) From 17 cases of clouds over tundra, the bias is small, being 5.8 W m^{-2}, which indicates a good agreement between computed irradiances based on the retrieval results and ground-based observed irradiances.

2) From 12 cases of clouds over snow/ice, the bias is -5.1 W m^{-2}, which shows a good agreement between the inferred and observed irradiances. The higher rms deviation for the tundra cases indicates larger error in the retrieved cloud parameters.

3) From the nine cases in which we compare cloud-top temperature to sounding data, the rms deviation and bias are 2.4 and 0.03 K, respectively. Thus, there is good agreement between the retrieved cloud-top temperature and the sounding data.

To test the physical soundness and illustrate the utility of our retrieval algorithms, we have analyzed AVHRR images taken over the North Slope of Alaska, the Beaufort Sea, and the Chukchi Sea representing different types of underlying surfaces to retrieve surface reflectance and cloud parameters. These results show the following.

1) For a tundra surface, channel 1 albedo is about 0.05 when the solar zenith angle is about 53°. Snow grain radius is found to be about 1000 μm for the specific time and location of the observations.

2) We find that water cloud droplet radii generally increase with optical thickness for optically thin clouds ($\tau < 20$) and decrease for optically thick clouds. From the cases analyzed in this study, clouds over the ocean exhibit a slightly negative correlation between these two quantities, whereas clouds over the tundra exhibit a clearly positive correlation between the two. Cloud over snow/ice, for which τ has a wider range than for ocean and tundra, have a positive correlation between the τ and r_e when $\tau < 20$ and a very weak negative correlation when $\tau > 20$.

3) In the specific case selected for cloud parameter retrieval, the effective radius of clouds over tundra lies between 4 and 11 μm, with a peak occurrence of 18%

at r_e about 7–8 μm. Over the ocean, the droplet size is slightly larger, lying between 6 and 12 μm with a peak occurrence close to 25% at r_e about 9–10 μm, which is consistent with that in mid- and low latitudes. Over snow/ice, the effective radius lies between 5 and 12 μm, and the peak occurrence is about 17% at r_e about 10–11 μm. The retrieved cloud effective radius is generally smaller than at mid- and low latitudes, which is consistent with in situ measurements (Tsay and Jayaweera 1984).

We emphasize that the relationships between cloud optical properties inferred above are based on a small number of AVHRR scenes. Therefore, while they give physically reasonable results, a much larger sample would be needed to establish statistically robust relationships. AVHRR data collected in the Arctic Ocean as part of the ongoing Surface Heat Budget of the Arctic Ocean (SHEBA) experiment will provide an abundance of data that will allow us to further test and validate these algorithms by comparing retrieved results against SHEBA data including cloud microphysical properties inferred from ground-based radiometry as well as cloud radar and lidar measurements. A major climate research facility has just been established on the North Slope of Alaska as part of the Atmospheric Radiation Measurement (ARM) program (Stamnes et al., 1999) sponsored by the U.S. Department of Energy (DOE). Data collected at the North Slope of Alaska ARM facility similar to those collected at the SHEBA site are expected to be be very useful for validation purposes. In connection with the SHEBA and ARM efforts NASA has been conducting extensive aircraft campaigns to collect in situ cloud microphysical data over the ARM and SHEBA sites. Taken together these coordinated efforts by several federal agencies [NASA, National Science Foundation (NSF) and Office of Naval Research (SHEBA), and DOE (ARM)] will provide a wealth of valuable data that can be used for remote sensing validation in the future.

The sloped nature of the snow surface can be important for the correct retrieval of surface properties, and this feature should be accounted for in areas where the surface slope is significant. Also, we have based our retrieval on a plane-parallel radiative transfer model. This choice is based on the experience that arctic stratus clouds tend to be horizontally stratified (Tsay and Jayaweera 1984). In the future, cloud heterogeneity effects may have to be considered for very large solar zenith angles as discussed by Welch and Wielicki (1989) and Loeb and Davies (1997).

Finally, there are several practical aspects that must be considered from an operational point of view: (i) a procedure to classify each pixel as clear versus cloudy is needed; (ii) if a pixel is classified as clear, one must determine the nature of the underlying surface, that is, snow versus tundra, and so on. Once these classifications have been established the algorithms discussed in this paper can be used to construct operational cloud/surface retrieval algorithms. From an operational point of view there is also a need to establish a procedure to identify clear pixels in an automated manner. For this purpose an automated cloud detection and classification technique (Lubin and Morrow 1998), relying on multispectral and pattern recognition techniques (Ebert 1987) may be used to provide results on an operational basis. These important operational issues are left for future consideration and resolution.

Acknowledgments. We are grateful to Robert H. Whritner and Elizabeth A. Nelson of the Arctic and Antarctic Research Center for their help with satellite data collection and processing, to Si-Chee Tsay at NASA/Goddard Space Flight Research Center for help with the radiative transfer model, and to Kevin Engle at University of Alaska, Fairbanks, for his help with the use of the TeraScan system. We thank Steve Warren and two anonymous reviewers for constructive criticism that helped improve the quality of this paper. This work was supported by the National Science Foundation through Grant OPP91-140010 to the University of Alaska and by the Environmental Sciences Division of the U.S. Department of Energy (DOE Contract 091574-A-Q1 to the University of Alaska) as part of the Atmospheric Radiation Measurement program.

REFERENCES

Albrecht, B. A., 1989: Aerosols, cloud microphysics and fractional cloudiness. *Science,* **245,** 1227–1230.

Blanchet, J., and R. List, 1983: Estimation of optical properties of arctic haze using a numerical model. *Atmos.–Ocean,* **21,** 444–465.

Brandt, R. E., T. C. Grenfell, and S. G. Warren, 1991: Optical properties of snow. *Antarct. J. U. S.,* **26,** 272–275.

Brest, C. L., and W. B. Rossow, 1992: Radiometric calibration and monitoring of NOAA AVHRR data for ISCCP. *Int. J. Remote Sens.,* **13,** 235–273.

Clarke, A. D., and K. J. Noone, 1985: Soot in the Arctic snowpack: A cause for perturbations in radiative transfer. *Atmos. Environ.,* **19,** 2045–2053.

Curry, J. A., and G. F. Herman, 1985: Infrared radiative properties of summertime arctic stratus clouds. *J. Appl. Meteor.,* **24,** 525–538.

de Abreu, R. A., J. Key, J. A. Maslanik, M. C. Serreze, and E. F. LeDrew, 1994: Comparison of in situ and AVHRR-derived broadband albedo over Arctic sea ice. *Arctic,* **47,** 288–297.

Dutton, G. E., and J. R. Christy, 1992: Solar radiative forcing at selected loations and evidence for global lower tropospheric cooling following the eruptions of El Chichón and Pinatubo. *Geophys. Res. Lett.,* **19,** 2313–2316.

Ebert, E., 1987: A pattern recognition technique for distinguishing surface and cloud types in the polar regions. *J. Climate Appl. Meteor.,* **26,** 1412–1427.

Eck, T. F., D. W. Deering, and L. A. Vierling, 1997: Arctic tundra albedo and its estimation from spectral hemispheric reflectance. *Int. J. Remote Sens.,* **18,** 3535–3549.

Forster, P. M. F., and K. P. Shine, 1995: A comparison of two radiation schemes for calculating ultraviolet radiation. *Quart. J. Roy. Meteor. Soc.,* **121,** 1113–1131.

Grenfell, T. C., and D. K. Perovich, 1984: Spectral albedos of sea ice and incident solar irradiance in the southern Beaufort Sea. *J. Geophys. Res.,* **89,** 3573–3580.

——, S. G. Warren, and P. C. Mullen, 1994: Reflection of solar radiation by the Antarctic snow at ultraviolet, visible, and near-infrared wavelengths. *J. Geophys. Res.,* **99,** 18 669–18 684.

Han, Q., W. B. Rossow, and A. A. Lacis, 1994: Near-global survey of effective droplet radius in liquid water clouds using ISCCP data. *J. Climate,* **7,** 465–497.

Han, W., Z. Jin, and K. Stamnes, 1993: A model study on predicting surface bidirectional reflectances. *Eos, Trans. Amer. Geophys. Union,* **74.**

Henyey, L. G., and J. L. Greenstein, 1941: Diffuse radiation in the galaxy. *Astrophys. J.,* **93,** 70–83.

Hu, Y. X., and K. Stamnes, 1993: An accurate parameterization of the radiative properties of water clouds suitable for use in climate models. *J. Climate,* **6,** 728–742.

Kaufman, Y. J., and B. N. Holben, 1993: Calibration of the AVHRR visible and near-IR bands by atmospheric scattering, ocean glint, and desert reflection. *Int. J. Remote Sens.,* **14,** 21–52.

Key, J., 1996: The Cloud and Surface Parameter Retrieval (CASPR) system for polar AVHRR, Version 1.0: User's guide. Department of Geography, Boston University, 73 pp. [Available from Department of Geography, Boston University, 625 Commonwealth Ave., Boston, MA 02215.]

——, 1999: The Cloud and Surface Parameter Retrieval (CASPR) System User's Guide. Tech. Rep. 96-02, Department of Geography, Boston University, 56 pp. [Available from Department of Geography, Boston University, 625 Commonwealth Ave., Boston, MA 02215.]

——, and M. Haefliger, 1992: Retrieval of ice surface temperature, outgoing longwave radiation, and cloud cover from AVHRR data. WMO Report on Polar Radiation Fluxes and Sea Ice Modeling, World Meteorological Organization, WCRP-62, WMO/TD-442, C22-C28.

Kidwell, K. B., 1995: NOAA polar orbiter data user's guide. NOAA/NESDIS/NCDC. [Available from NOAA/NESDIS, 4401 Suiteland Rd., Rm. 2069, Suiteland, MD 20233.]

King, M. D., 1987: Determination of the scaled optical thickness of clouds from reflected solar radiation measurements. *J. Atmos. Sci.,* **44,** 1734–1751.

Latimer, J. R., 1972: Radiation measurement. International Field Year for the Great Lakes. Tech. Manual Series 2, National Research Council of Canada, Ottawa, ON, Canada, 53 pp. [Available from National Research Council of Canada, Ottawa, Ontario K1A 0R6 Canada.]

Leaitch, W. R., J. W. Strapp, H. A. Wiebe, and G. A. Isaac, 1983: Measurements of scavenging and transformation of aerosol inside cumulus. *Precipitation Scavenging, Dry Deposition, and Resuspension,* H. R. Pruppacher, R. G. Semonin and W. G. N. Slinn, Eds., Elsevier, 53–66.

List, R. J., 1968: *Smithsonian Meteorological Tables.* Smithsonian Institution, 527 pp.

Loeb, N. G., 1997: In-flight calibration of NOAA AVHRR visible and near-IR bands over Greenland and Antarctica. *Int. J. Remote Sens.,* **18,** 477–490.

——, and R. Davies, 1997: Angular dependence of observed reflectances: A comparison with plane parallel theory. *J. Geophys. Res.,* **102,** 6865–6881.

Lubin, D., and P. J. Weber, 1995: The use of cloud reflectance functions with satellite data for surface radiation budget estimation. *J. Appl. Meteor.,* **34,** 1333–1347.

——, and E. Morrow, 1998: Evaluation of an AVHRR cloud detection and classification method over the central Arctic Ocean. *J. Appl. Meteor.,* **37,** 166–183.

——, P. Ricchiazzi, C. Gautier, and R. H. Whritner, 1994: A method for mapping Antarctic surface ultraviolet radiation using multispectral satellite imagery. *Radiation in Antarctica: Measurements and Biological Effects,* Amer. Geophys. Union Antarctic Research Series, Vol. 62, Amer. Geophys. Union, 166–183.

McClatchey, R. A., R. W. Fenn, J. E. A. Selby, F. E. Volz, and J. S. Garing, 1971: Optical properties of the atmosphere. Air Force Cambridge Rep. AFGRL-71-0279, 85 pp.

Nakajima, T., and M. D. King, 1990: Determination of the optical thickness and effective particle radius of clouds from reflected solar radiation measurements. Part I. Theory. *J. Atmos. Sci.,* **47,** 1878–1893.

——, ——, J. D. Spinhirne, and L. F. Radke, 1991: Determination of the optical thickness and effective particle radius of clouds from reflected solar radiation measurements. Part II: Marine stratocumulus observations. *J. Atmos. Sci.,* **48,** 728–750.

Nakajima, T. Y., and T. Nakajima, 1995: Wide-area determination of cloud microphysical properties from NOAA AVHRR measurements for FIRE and ASTEX regions. *J. Atmos. Sci.,* **52,** 4043–4059.

Penndorf, R., 1957: Tables of the refractive index for standard air and the Rayleigh scattering coefficient for the spectral region between 0.2 and 20 μm and their application to atmospheric optics. *J. Opt. Soc. Amer.,* **47,** 176–182.

Pinker, R. T., and I. Laszlo, 1992: Modeling surface solar irradiance for satellite applications on a global scale. *J. Appl. Meteor.,* **31,** 194–211.

Platnick, S., and S. Twomey, 1994: Determining the susceptibility of cloud albedo to change in droplet concentration with the Advanced Very High Resolution Radiometer. *J. Appl. Meteor.,* **33,** 334–347.

——, and F. P. J. Valero, 1995: A validation study of a satellite cloud retrieval during ASTEX. *J. Atmos. Sci.,* **52,** 2985–3001.

Rao, C. R. N., and J. Chen, 1995: Inter-satellite calibration linkages for the visible and near-infrared channels of the Advanced Very High Resolution Radiometer on the NOAA-7, -9, and -11 spacecraft. *Int. J. Remote Sens.,* **16,** 1931–1942.

Rossow, W. B., L. C. Gardner, and A. A. Lacis, 1989: Global seasonal cloud variations from satellite radiation measurements. Part I: Sensitivity of analysis. *J. Climate,* **2,** 419–458.

Saunders, R. W., 1990: The determination of broad band surface albedo from AVHRR visible and near-infrared radiances. *Int. J. Remote Sens.,* **11,** 49–67.

Shaw, G., 1982: Atmospheric turbidity in the polar regions. *J. Appl. Meteor.,* **21,** 1080–1088.

Shettle, E. P., and R. W. Fenn, 1976: Models of atmospheric aerosols and their optical properties. *Optical Propagation in the Atmosphere,* Agard Conference Proceedings 183, AGARD-CP-183, [NTIS ADA 028615.]

Stamnes, K., and S.-C. Tsay, 1990: Optimum spectral resolution for computing atmospheric heating and photodissociation rates. *Planet. Space Sci.,* **38,** 807–820.

——, ——, W. Wiscombe, and K. Jayaweera, 1988: Numerically stable algorithm for discrete-ordinate-method radiative transfer in multiple scattering and emitting layered media. *Appl. Opt.,* **24,** 2502–2509.

——, R. G. Ellingson, J. A. Curry, J. E. Walsh, and B. D. Zak, 1999: Review of science issues, deployment strategy, and status for the ARM North Slope of Alaska–Adjacent Arctic Ocean Climate research site. *J. Climate,* in press.

Stuhlmann, R., and P. Bauer, 1990: Retrievals of radiation from satellite data and aircraft measurements. WMO Report on Polar Radiation Fluxes and Sea Ice Modeling, World Climate Research Programme, WCRP-62, WMO/TD-442.

Suttles, J. T., R. N. Green, P. Minnis, and G. L. Smith, 1988: Angular radiation models for earth atmosphere system. NASA Ref. Publ. 1184, 143 pp. [Available from NASA, 300 E. St. SW, Washington, DC 20546.]

Taylor, V. R., and L. L. Stowe, 1984: Atlas of reflectance patterns for uniform earth and cloud surfaces (NIMBUS-7ERB-61 days). NOAA Tech. Rep. NESDIS 10, 66 pp. [Available from NOAA/NESDIS, 4401 Suiteland Rd., Rm. 2069, Suiteland, MD 20233.]

Teillet, P. M., P. N. Slater, Y. Ding, R. P. Santer, R. D. Jackson, and M. S. Moran, 1990: Three methods for the absolute calibration of the NOAA AVHRR sensors in-flight. *Remote Sens. Environ.,* **31,** 105–120.

Tsay, S.-C., and K. Jayaweera, 1984: Physical characteristics of arctic stratus clouds. *J. Climate Appl. Meteor.,* **23,** 584–596.

——, K. Stamnes, and K. Jayaweera, 1989: Radiative energy budget in the cloudy and hazy Arctic. *J. Atmos. Sci.,* **46,** 1002–1018.

——, ——, and ——, 1990: Radiative transfer in stratified atmospheres: Development and verification of a unified model. *J. Quant. Spectrosc. Radiat. Transfer,* **43,** 133–148.

Turco, R. P., R. C. Whitten, and O. B. Toon, 1982: Stratospheric aerosols: Observation and theory. *Rev. Geophys. Space Phys.,* **20,** 233–279.

Twomey, S., and T. Cocks, 1982: Spectral reflectance of clouds in the near-infrared: Comparison of measurements and calculations. *J. Meteor. Soc. Japan,* **60,** 583–592.

——, and ——, 1989: Remote sensing of cloud parameters from spectral reflectance in the near-infrared. *Beitr. Phys. Atmos.,* **62,** 172.

Valero, F. R. J., T. P. Ackerman, and W. J. Y. Gore, 1983: Radiative effects of the arctic haze. *Geophys. Res. Lett.,* **10,** 1184–1187.

Wang, P., and J. Lenoble, 1994: Comparison between measurements and modelling of UV-B irradiance for clear sky—A case study. *Appl. Opt.,* **33,** 3964–3971.

Warren, S. G., and W. J. Wiscombe, 1980: A model for the spectral albedo of snow. Part II: Snow containing atmospheric aerosols. *J. Atmos. Sci.,* **37,** 2734–2745.

——, and ——, 1985: Dirty snow after nuclear war. *Nature,* **313,** 467–470.

Welch, R. M., and B. A. Weilicki, 1989: Reflected fluxes for broken clouds over a Lambertian surface. *J. Atmos. Sci.,* **46,** 1384–1395.

Wiscombe, W. J., and S. G. Warren, 1980: A model for the spectral albedo of snow. Part I: Pure snow. *J. Atmos. Sci.,* **37,** 2712–2733.

Zeng, J., R. McKenzie, K. Stamnes, M. Wineland, and J. Rosen, 1994: Measured UV spectra compared with discrete ordinate method simulations. *J. Geophys. Res.,* **99,** 23 019–23 030.